Eindhoven University of Technology

Eindhoven University of Technology

MASTER

Chlamydomonas Reinhardtii
from microscopic swimming to macroscopic rheology

Boesten, R.J.J.

Award date:
2011

Link to publication

Chlamydomonas Reinhardtii: from microscopic swimming to macroscopic rheology

R.J.J. Boesten
June 9, 2011

Abstract

The unicellar green alga *Chlamydomonas* Reinhardtii has two flagella with which it performs a 'breaststroke' like movement to propel itself. This alga is currently investigated for industrial purposes on the macroscale, and has recently drawn attention by physical experiments on the microscale of a single organism. This thesis aims to give an insight in both the swimming behaviour of a single alga and the influence of swimming at the macroscopic properties of suspensions of many algae. The simple analytic three-point-force model and a qualitative analysis of the flagellar stroke reproduces the experimentally obtained flow fields of Guasto et al. [23]. Two new derivations are presented for the effective viscosity of a dilute suspension of *Chlamydomonas* cells. Both are in agreement with previous theoretical results. The effective viscosity depends on the average swimming direction of the algae. A literature study on the ordering of active suspensions leads to the conclusion that swimming results in an increase of the viscosity for small shear rates, for higher shear rates it is undistinguishable compared to a passive suspension.

Contents

Chapter 1

Introduction in the microswimmer world

There is an abundancy of life on almost every part of our planet, from penguins on the icy south pole to cactuses in the dry hot deserts and fish in the deepest oceans. This diversity is not limited to the macroscopic world, visible to our naked eye. When one takes a look with a microscope in the micrometer world, one finds countless fungi, algae, viruses, bacteria, etc. Within our own body spermatozoa can be regarded as independent acting 'microorganisms'. Many of these microscopic unicellular life forms propel themself in search for a better environment. They may seek the ovum (egg cell), look for the right light intensity or try to get rid of toxic chemicals in their neighbourhood. There are several propelling mechanisms, which all have in common that they are neither coordinated nor regulated by a brain. Although a lot is known about genetics and cell architecture of microorganisms, the motility of eukaryotes[1] is not yet fully understood. All animals, plants, fungi and protists are eukaryotes. We owe our existence to microswimming, without a beating flagellum a sperm cell will never reach the ovum. On the other hand microswimmers can cause lethal effects in humans, the African Tripanosome (figure 1.1) swimming in the blood stream causes a feared disease known as sleeping sickness.

The extensively studied *Chlamydomonas* Reinhardti, see figure 1.1, is an eukaryote. This green unicellular alga has two flagella protruding at the front of its body performing a 'breast-stroke'. Its swimming movement was already recorded in detail 25 years ago [61], but has recently drawn attention by experiments conducted on the flow fields induced by swimming on micrometer length and millisecond time scales [23, 18]. On macroscopic length and timescales viscosity measurements on suspensions of *Chlamydomonas* have been performed [59]. There are currently many research projects on algae (among which *Chlamydomonas*), e.g. as a biofuel producer [48], as a basis for coating [32] and as a basis for feed [31]. Over the last 40 years, theoretical research has succesfully treated microswimming in a general way, describing its influence on macroscopic length scales [63, 26], or by using theoretical swimmers on small length scales [47, 33, 43, 50]. Nonetheless, existing theories do not explain the recent experimental findings on *Chlamydomonas* on both small and large length scales. The recent experimental observations and various emerging industrial applications of *Chlamydomonas* require a more thorough and species specific treatment of microswimming.

Microswimming is a fairly new field of physics, which is generally unknown to most physicists. Therefore a general introduction in this topic is provided as background material in the next

---

[1]Eukaryotic cells have a membrane and a nucleus.
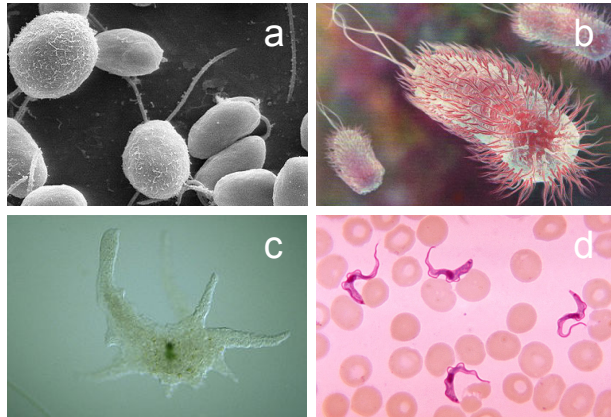
Figure 1.1: a) *Chlamydomonas* Reinhardtii, a green alga with two flagella [65]. b) The bacteria Escheria Coli, which can cause food poisoning, rotates a bundle of passive flagella [53]. c) Amoebes propel themself by altering their bodyshape [65]. d) African Tripanosomes between red blood cells [65].

chapter. It is based on the inspiring work "Life at low Reynolds number" by Purcell [58] and the recent review paper by Lauga et al. [42]. For those readers familiar with the field of low Reynolds number swimming, you might want to start reading chapter 3.

The major part of this thesis is divided into two parts. In chapter 3 the swimming motion of a single cell is considered on a length scale of micrometers, in chapter 4 the properties of suspensions of many cells is considered at large, laboratory length scales. The research questions which are addressed in this thesis are:

- How can the flow fields induced by swimming of *Chlamydomonas* be modeled?

- What effect does microswimming have on the viscosity of a suspension of *Chlamydomonas* cells?

The first question is addressed in chapter 3 by qualitative analysis of the movement of the flagellum and employing the analytic three-point-force model, it is especially motivated by the experiments of Drescher et al. [18] and Guasto et al. [23]. The simple model reproduces the not yet understood experimental flow fields. Chapter 4 is devoted to the last question, where two new derivations are presented for the effective viscosity of suspensions of swimming *Chlamydomonas*, which turns out to depend on the orientation of the cells. Furthermore, a review of theoretical and numerical work is provided on orientation mechanisms for passive and active suspensions. Finally, the theoretical results are compared to the experimental data of Rafai et al. [59].

Chapter 2

General physics of microswimming

2.1 Hydrodynamics at low Reynolds number

Although the size of the extensively studied $2\,\mu$m long E. Coli [65] bacterium and the $400\,\mu$m long Volvox [18] differs by two orders of magnitude, they are both considered microswimmers in literature. Throughout this work we consider *Chlamydomonas* as our typical model microswimmer. It has a spherical cell body with a radius $a \sim 10\,\mu$m and swims with a speed $U \sim 100\,\mu$m/s. For comparison, the thickness of a human hair is about $100\,\mu$m and the thickness of food foil is typically 15μm. Although we could swim in the same pool as *Chlamydomonas*[1], we would encounter a very different environment. This can be illustrated with the Reynolds number, which is the ratio of inertial over viscous forces. For a suspended body of size L and swimming with speed U it is given by

$$Re = \frac{F_{inertial}}{F_{viscous}} = \frac{LU\rho}{\eta}\,, \tag{2.1}$$

where ρ and η are the mass density and viscosity of the fluid. Reynolds numbers for different organisms and objects are listed in figure 2.1. Swimming humans have a Reynolds number of $Re \sim 10^4$. Once we stop swimming in the pool, we coast for several meters [42]. However for a microswimmer ($Re \sim 10^{-3}$) to stop swimming in the pool means coming to a stand still within $t_s = 0.5$ ms covering a distance of only $0.01\,\mu$m or 10^{-3} body length. To imagine what swimming under these conditions would be, you should think of floating around in a pool filled with molasses and being allowed to move any part of your body with a speed of less than a centimer per minute [58].

For small Reynolds numbers ($Re \ll 1$) the inertial terms in the Navier-Stokes equation can be neglected and fluid motion is described by the Stokes equation (see appendix C)

$$\nabla p + \eta\nabla^2\vec{u} = \vec{F}\,, \tag{2.2}$$

with p the pressure, $\vec{F}$ the external forces per unit volume and $\vec{u}$ the velocity of the fluid. There is no time dependency in (2.2), the fluid motion at any time is fully determined by the boundary conditions at that exact moment, i.e. there is no history dependence and there exists a linear relation between friction force and velocity. The absence of diffusive, convective and

---

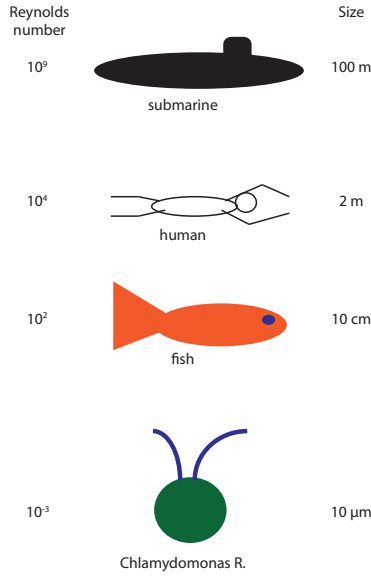[1] An experiment many of us have done unknowingly

Figure 2.1: The ratio of inertial forces and viscous forces (Reynolds number) for different swimming creatures and objects.

time dependent terms in (2.2) allows us to describe the flow as a superposition of elementary solutions, or Green's functions, of the Stokes equation.

Let us consider an infinitely small particle submerged in an unbound fluid, with the density of the particle exceeding the fluid density, thus gravity exerting a net force $\vec{F}$. Due to this force the particle translates in the direction of the gravitational field. The flow field created by this motion is the stokeslet, and is obtained by solving eq. (2.2) for a point force or force monopole, see figure 2.2 (left). Let us now consider a small torque-free and force-free, neutrally buoyant swimmer. It exerts two forces in opposite directions on the fluid e.g. a spermatozoa exerts a force on the fluid opposite to the swimming direction and an equal force is exerted by the cell body on the fluid along the swimming direction. In a coarse grained way it can be considered as a force dipole. Solving again eq. (2.2) for vanishing swimmer size yields the stresslet solution due to a pure dipole, as displayed in figure 2.2 (middle). Pullers are swimmers where the forces point inwards, like *Chlamydomonas*, for pushers like *E. Coli* the forces point outwards. The resulting flow field is the same, except for a sign change. The stokeslet and stresslet are the first two contributions of a multipole expansion, which can be extended by taking into account quadrupoles, octopoles, etc. Any flow field at low Reynolds number can be written as a superposition of stokeslets, stresslets, source doublets [56], etc.

$$\vec{u}(\vec{r}) = \vec{u}_{stokeslet} + \vec{u}_{stresslet} + \vec{u}_{source\ doublet} + ... \qquad (2.3)$$

The source doublet is the leading term in the flow field for a force quadrupole, see figure 2.3. It is for example created by *Chlamydomonas* in the configuration shown in figure 2.2(right). A mathematical description of the velocity fields and multipole expansion is presented in appendix C.

Flow at the dimensions of microorganisms is fully determined by the boundary conditions, inertia plays no role and flow fields can be described by a superposition of elementary flow fields.

7
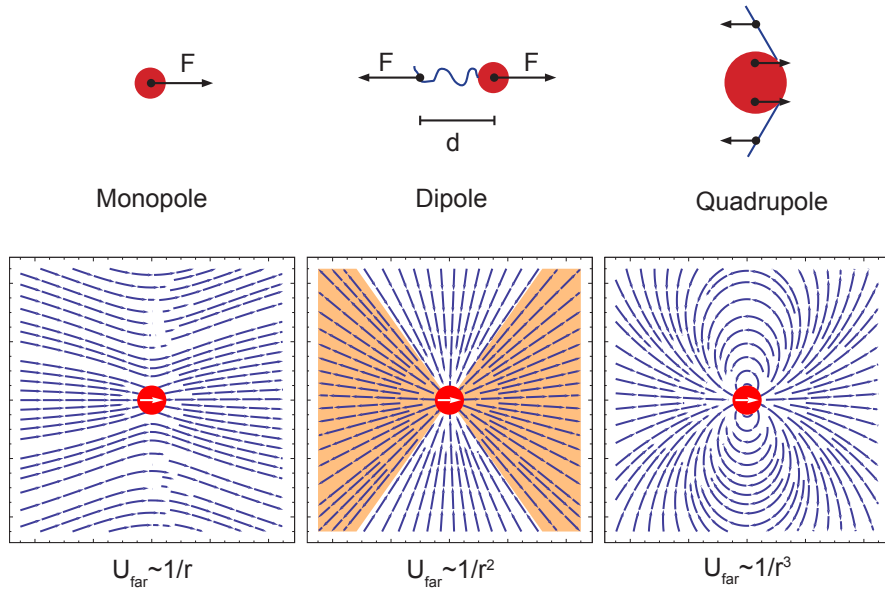
Figure 2.2: Three elementary flow fields and their far field. (left) A force monopole or point force creates a stokeslet flow. (middle) A dipole as induced by e.g. a spermatozoa creates a pusher stresslet field. The field lines in the blank and shaded orange area point outwards and inwards, respectively. (right) A force quadrupole induces a source doublet flow in first order.

Figure 2.3: A source doublet with a sink (left) and a source (right).

8
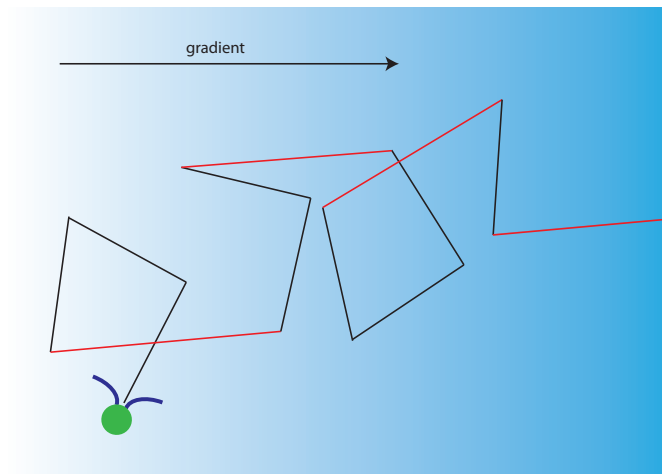
Figure 2.4: A gradient in left-right direction (nutrients, toxic chemicals, etc.) creates a preferred swimming direction. Darker color indicates a more favorable condition for the organism. When the organism swims in the direction of the gradient, it continues swimming in this direction for a longer period of time (red lines).

2.2 Scallop theorem

The time indepencence of the Stokes equation restricts the possible swimming motions. This was elucidated by Purcell [58] with the so-called scallop theorem: a scallop opens its clam slowly and closes it fast, squirting out water. In the high Reynolds number environment this leads to a net displacement after one opening/closing cycle, but at low Reynolds number it would end up at its exact starting position. This is due to the reciprocal motion of the scallop, a movie of one cycle played backwards looks the same as the movie itself. The time independence of the Stokes equation implies that no matter how fast or slow you move, as long as the Reynolds number remains small, a reciprocal motion does not result in a net displacement. The micro scallop with one degree of freedom (open/close) is not capable of performing a non-reciprocal motion. All microswimmers perform a non-reciprocal movement, for *Chlamydomonas* this will be elucidated in chapter 3.

2.3 Brownian motion, diffusion and random walks

Fluid particles are in constant motion, whereby the average velocity increases with temperature. These fluid particles collide with suspended objects, creating a random movement of the (small) suspended particles, this is called Brownian motion. Brownian motion results in diffusion of the suspended particle and is described by a diffusion constant for a spherical particle with radius R given by the Stokes-Einstein relation [19]

$$D = \frac{kT}{6\pi\eta R},$$ (2.4)

with T the temperature and k the Boltzmann constant. The Peclet number is the ratio of times a particle needs to diffuse a distance L compared to travel the same distance by ballistic motion $Pe = RU/D$. At room temperature ($T = 300\,\text{K}$) in water ($\eta_{water} = 1\,\text{mPa}\cdot\text{s}\cdot\text{m}$) the Peclet

number for the typical microswimmer is $Pe \simeq 10^8$, which makes clear that diffusive motion is negligible for the typical microswimmer. This is no surprise, if you would travel as fast by doing nothing as you would by actively swimming, then why would you swim? The rotary diffusion constant for a sphere is given by the Stokes-Einstein relation

$$D_r = \frac{k_B T}{8\pi \eta R^3} .$$
(2.5)

The reciprocal rotary diffusion constant for a typical microswimmer is $1/D_r \sim 8 \cdot 10^2$ s, where again water is used as a suspending medium at room temperature. This indicates that at lab timescales $(0.001 - 10)$s the swimmer (rotary) diffusion is negligible. Many microswimmers use a simple algorithm to 'scan' their environment. They swim in a straight line for a time t_s and after this time decide to:

- 1. Randomly change direction if conditions have not improved [2]

- 2. Remain swimming in the same direction if conditions have improved

This results in a biased random walk [28], see figure 2.4. In this way the organism probes its vicinity for food, toxic chemicals etc. On longer time scales, i.e. after many reorientation events, a random walk can be described as effective diffusion. For suspensions of *Chlamydomonas* the effective diffusion constant was obtained experimentally as $D_{eff} = 7 \cdot 10^{-8}$ m/s^2 and $D_{eff}/D \sim 10^6$ [55]. The effective rotary diffusion is $D_{r,eff} = 0.4$ rad^2/s [35] and $D_{r,eff}/D_r \sim 400$.

Microswimmers search for food molecules. The typical size of these biological molecules soluted in water is ~ 10 nm. To out-swim diffusion microswimmers have to travel a length scale $l_{diff} = D_{bio}/U \sim 100$ μm [58], where D_{bio} is the diffusion constant of the biological molecules. This is the typical length after which *Chlamydomonas* changes its direction.

The diffusion of a microswimmer is negligible compared to the swimming speed. They scan their environment via a simple random walk algorithm, whereby they outrun diffusion of nutrients, chemicals, etc.

2.4 Flagellar propulsion

Amoebes change their body shape and bacteria use a motor to rotate a passive bacterial flagellum to propel themselves [42]. But all eukaryotic microswimmers use one or more active flagella for the propulsion of their body, see figure 2.5. These flagella have the same basic structure as displayed in figure 2.6 which is thought to originate from the mutual eukaryotic ancestor about 1-2 billion years ago [52].

The flagellum consists of 2 central microtubuli and 9 outer microtubuli doublets, covered by a flagellar membrane. The central pair is surrounded by a structure called the central pair apparatus, it is connected with the outer microtubuli doublets via radial spokes which seem to play a role in altering and regulating the flagellar beat [25]. The dynein motors are connected to the A microtubulus and reach out to the B microtubulus of the next doublet. Within a single flagellum over 16 different motors have been reported and the total number of motors in a *Chlamydomonas* flagellum is about 10.000 [25]. The microtubuli are hollow tubes with a diameter of 25 nm, their bending rigidity is about $k_m = 3 \cdot 10^{-23}$ Nm^2 [1]. In multicellular organisms like humans, one finds flagella in the spermatozoa, in lungs and throat for dust removal and even the left-right asymmetry of our body is caused by the beating of flagella on the surface of the

---

[2]The reorientation is not perfectly random: their usually exists a correlation between consecutive swimming directions which is species dependent.
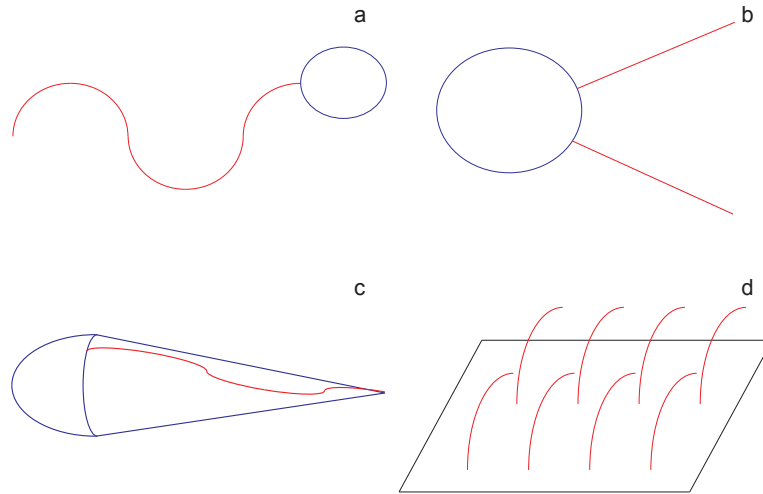
Figure 2.5: a) Spermatozoa have a flagellum attached to their back (with respect to the swimming direction). b) *Chlamydomonas* has two flagella protruding from the front of its body, c) African Tripanosomes have a flagellum which is over the full length of its body attached to the cell. d) An array of cilia which can be found in the respiratory tract of the human body and other mammals.
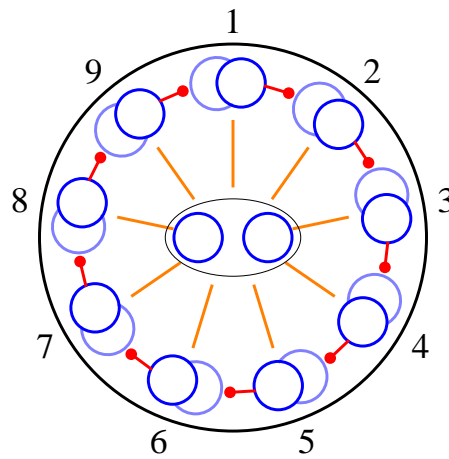
Figure 2.6: Schematic overview of a 9+2 flagellum. The central pair microtubuli (inner blue circles) are surrounded by the central pair apparatus (ellipse). 9 outer microtubuli doublets form a ring, they are numbered 1-9 by convention. The dark and light blue parts are the A and B microtubulus respectively. The dynein motors (red) originate at the A microtubulus and extend towards the B microtubulus of the next doublet. The radial spokes (orange) originate at the A microtubulus too, they are connected with the central pair apparatus.
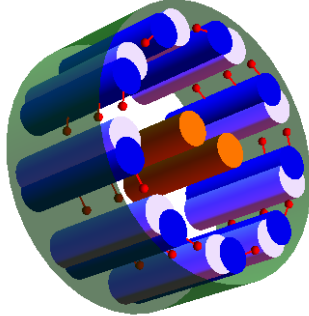
Figure 2.7: Schematic 3D overview of a segment of 96 nm of the axoneme. The flagellum consists of 1-10000 of these connected segments.

(a)   (b)

Figure 2.8: Schematic overview of dynein activity. a) Two microtubuli (blue) are parallel to each other. When the dynein motors are switched on, the two microtubuli start sliding in the direction depicted by the two orange arrows. b) The dynein motors have induced sliding, but no bending has occurred.

embryo [25]. Within the body flagella, when they come in arrays and when they are relatively short, are called cilia, but their design is the same except for the non-existing central pair, the 9+0 flagella/cilia. The length of flagella ranges from $1\,\mu$m for the smallest cilia to $58000\,\mu$m [52] in the spermatozoa of fruit flies[3]. The diameter of the flagellum is constant along the flagellum ($200\,\mu$m). For *Chlamydomonas* the flagella consist of repeating segments of 96 nm as displayed in figure 2.7.

The dynein motors which are located on all 9 microtubuli doublets are most probably unidirectional [25, 12]. The motors on microtubuli i can push microtubuli $i-1$ in the direction of the cell body. The dynein activity on itself does not create a bend but merely results in sliding, as illustrated in figure 2.8. Geometrical constraints, created by the attachment to the cell body and the flagellar structure, are necessary to turn this sliding movement into a bend. This is illustrated in figure 2.9. The organisms considered are unicellular and may have more than 100.000 dynein units, but still manage to create complex and sustainable beating patterns. Camalet et al. [14] treated the motors as oscillators and showed that regardless of the microscopic architecture and switching mechanism a series of oscillators is able to create a sustainable beating pattern. Several motor control mechanisms have been proposed [45, 11], succesfully reproducing beating patterns

---

[3]it exceeds their bodylength of 1 mm

(a)   (b)
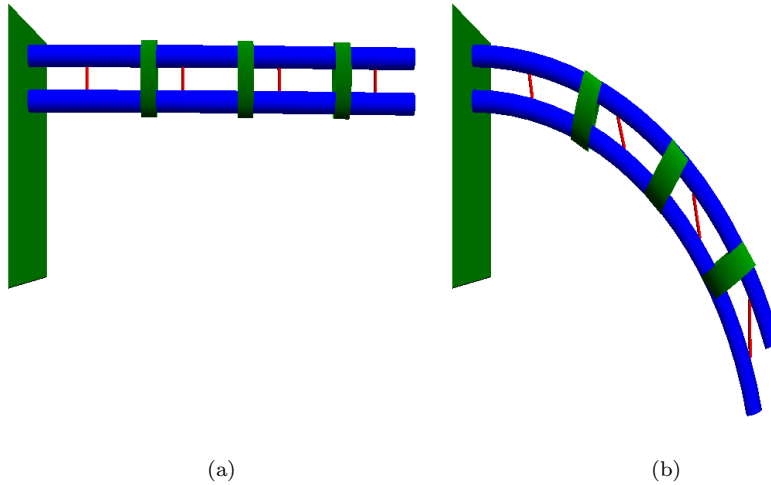
Figure 2.9: a) Two microtubuli (blue) are connected to a wall (green sheet) and additional geometrical constraints (green rings) apply. b) The dynein motors (red) are switched on and exert a force, due to the rigid connection to the wall and the geometrical constraints, the motor activity creates a bend. The length of the microtubuli and the distance between the centerlines of both tubes is conserved.

for a limited number of organisms. Until now the exact mechanism remains a mystery, as concluded by several recent reviews [25, 12, 66, 46]. Many organisms perform a random walk which is biased by chemicals, nutrients, light intensity etc. This indicates that these organisms have chemical and light sensors which influence the flagellar movement. Eukaryotic microswimmers propel themselves with flagella, containing many internal motor units. The control mechanism for the motors is yet unknown.

2.5 Theoretical models

Several theoretical microswimmers have been proposed, which give insight in swimming at low Reynolds number. Investigations range from swim efficiency [44, 8], wall interactions [47], to influence of phase difference of cyclic swimmers [2] and swimmer-swimmer interaction of a few [34] or many swimmers [33]. The most important microswimmer models are:

- **Taylor sheet** An oscillating sheet was shown to move by Taylor [64] as early as 1951.

- **Najafi-Golestanian swimmer** [50] Three spheres in a row are connected by two linkers, hence it is also known as a two link swimmer. The two links create two degrees of freedom, allowing for non reciprocal movement.

- **Squirmer** Introduced by Lighthill in 1952 [44] and later developed by Blake [8], it was used to model spherical swimmers which move by slightly altering their body shape, or for swimming bodies covered by arrays of beating cilia. The induced flow field is a superposition of the flow induced by a dipole force (stresslet) of strength B_2 and the flow induced by a force quadrupole of strength B_1. It is discussed in appendix F.

Chapter 3

The motion and induced flows of *Chlamydomonas* Reinhardtii

This chapter addresses the swimming motion and induced flows of a single *Chlamydomonas* cell on the micrometer length scale. First the cell characteristics and different motility modes are discussed in section 3.1 and 3.2. In section 3.3 the synchronisation of the two flagella is discussed and a new alternative hypothesis for the mechanism of synchronisation is presented. The experiments on the swimming induced flows are discussed in section 3.4. Finally I apply the three-point-force model to fully reproduce the experimentally obtained flows in section 3.5.
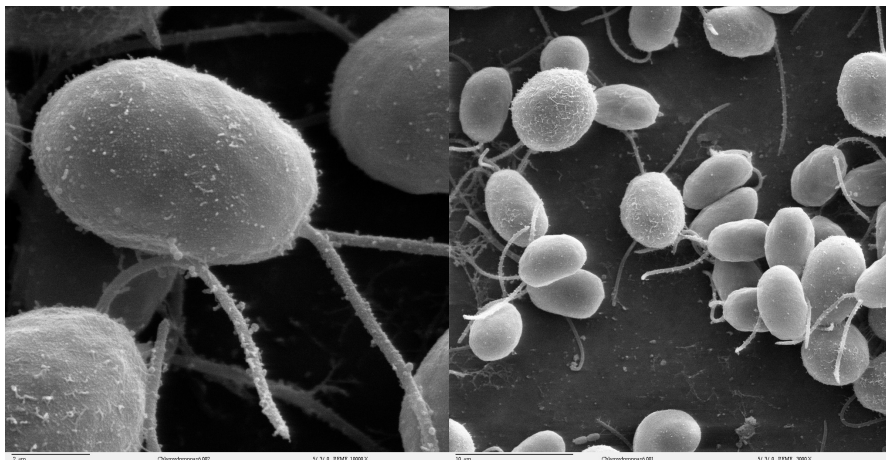

Figure 3.1: Electron microscopy images of *Chlamydomonas* Reinhardtii. Taken from [65].

3.1 Introducing *Chlamydomonas* - history and characteristics

The genus *Chlamydomonas* was already discovered in 1786 by Ehrenberg [25]. The different varieties discovered afterwards populate virtually every part of our planet. According to the

Table 3.1: Cell characteristic [37]

	Chlamydomonas	standard value used here
Cell aspect ratio	$1 - 1.5$	1.3
Cell diameter	$4 - 20\,\mu$m	$10\,\mu$m
Flagellar length	$4 - 20\,\mu$m	$12\,\mu$m
Flagellar diameter	$0.2\,\mu$m	
Flagellar angle	$0.6 - 1.5\,$rad	$0.7\,$rad
Flagellar bending rigidity		$6 \cdot 10^{-22}\,$Nm^2
Beat frequency	$40 - 60\,$Hz	$50\,$Hz
Cell density	$1.01 - 1.10\,$gcm^{-3}	$1.10\,$gcm^{-3}
Centre of gravity offset	$0 - 0.05$ body diameters	0.05 body diameters
Swimming speed	$0 - 200\,\mu$ms^{-1}	$40\,\mu$ms^{-1}

Chlamydomonas Sourcebook [25]:

"*Collection sites include temperate, tropical, and polar regions.* Chlamydomonas *species have been isolated from freshwater ponds and lakes, sewage ponds, marine and brackish waters, snow, garden and agricultural soil, forests, deserts, peat bogs, damp walls, sap on a wounded elm tree, an artificial pond on a volcanic island, mattress dust in the Netherlands, roof tiles in India, and a Nicaraguan hog wallow. A petri plate exposed for 1 minute from an airplane flying at 1100m altitude produced Chlamydomonas among other algae.* "

Although more than 500 species of *Chlamydomonas* have been described, *Chlamydomonas* Reinhardtii has gained the most interest by researchers. This green unicellar alga is non-lethal for humans. It can grow both in the light (whereby they use photosynthesis), and in the dark (when provided with acetate). Many different strains are available and can even be ordered online [15]. Cell size and other characteristics vary among different strains, see table 3.1, so one has to be cautious when comparing experiments.

A typical *Chlamydomonas* has an almost spherical cell body with a diameter of $\sim 10\,\mu$m, and two flagella (length $12\,\mu$m and diameter $0.2\,\mu$m) protruding at the front of its cell body. The side of the cell body where the flagella are attached is called the posterior side, the opposite side is the called the anterior side. The flagella extend $0.4\,\mu$m into the cell, and are anchored in the basal body. The latter will be discussed in section 3.3.

Chlamydomonas has a slightly higher density (5%) than water, which leads to sedimentation for dead cells. It is bottom heavy, so that gravity aligns the cells in the upward direction. *Chlamydomonas* uses photosynthesis as an energy source, it thus will look for the optimal light intensity. For this purpose it has a rudimentary photosensitive sensor called the eyespot at the front of its body. It is connected with the central pair of the flagellum.

3.2 The *Chlamydomonas* flagellum & motility modes

The bending rigidity of a single microtubulus has been measured: $30 \times 10^{-24}\,$Nm^2 [30]. We take the bending rigidity of the flagellum 20 times that of a single microtubulus: $A = 6.0 \times 10^{-22}\,$Nm^2, like in [14]. The persistence length of a flagellum is $l_p = A/(k_B T) = 0.14\,$m. As $l_p \gg L$ a passive flagellum behaves like a rigid rod and thermal fluctuations in the flagellum are negligible. The viscosity, length of the flagellum and bending rigidity define a characteristic relaxation time $t_{bend} = \frac{\eta L^4}{A} = 0.03\,$s. This is the typical time it takes for a bent rod to relax to its straight

equilibrium configuration in a viscous environment. Note that it is longer than the beat cycle time $t_{beat} \sim 0.02\,$s, during the beating cycle the flagellum is not able to relax to an equilibrium state. *Chlamydomonas* displays several motility modes:

- In the dark it swims the majority of the time along a tight helical path [55] between consecutive tumbling events. The distribution of the latter can be described by a Poisson process with an average time between tumbling events $t_t = 11\,$s [55]. The beat cycle consists of an effective stroke, where the cell body moves forward, and a recovery stroke, where the cell body moves backwards. These strokes differ in shape, thereby fullfilling the non-reciprocal constraint of low Reynolds number swimming. A schematic overview of the strokes is given in figure 3.2. Rueffer and Nultsch [61] and more recently Polin [55] have recorded the beating pattern. During the effective stroke the two flagella beat in plane. During the recovery stroke they beat partially out of plane. The latter is responsible for the rotation of the cell body with a frequency of $2\,$Hz [18] and the helical swimming path.

- After running straight for a certain period of time, *Chlamydomonas* reorientates or tumbles for a short period of time. It dephases its flagella, creating an irregular beating pattern. After $\sim 0.3\,$s the flagella are synchronised again. The asynchronous beating causes a random rotation of the cell body. On average in the dark cells swim straight for 95% of the time, the tumbling makes up for the remaining 5% of the time.

- An intense light flash or mechanical stimulus results in a photoshock response. After a short immotile period the flagella start beating in a different manner, it swims backwards instead of forwards.

- It can also use its flagella to creep or glide along surfaces of solid media [25], with an average speed of $1.6\,\mu$m/s. A useful property in the desert.

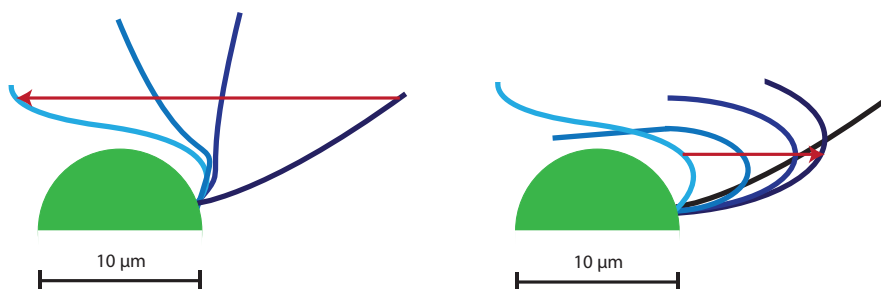Figure 3.2: Schematic overview of the swimming stroke. The effective stroke where the cell body moves forward (left) and the distal part of the flagellum is almost straight. The recovery stroke (right) in which the flagellum is strongly bend.

Chlamydomonas displays four distinct motility modes. The actual mode depends on time and environmental conditions. In this work the emphasis lays on the first, 'normal' mode.

3.3 Basal body and flagellar synchronisation

The flagella are attached to the cytoskeleton via the so-called basal body, see figure 3.3. The part of the flagellum closest to the cell body is called the basal part, the other side the distal part. Four bundles of microtubuli connect the basal parts of the flagella to the cytoskeleton. The flagella are connected to each other at their very end via the bundles of microtubuli, but also via the distal striated fiber. The angle between the flagella at their base has been studied by Brokaw [13] and Ringo [60] yielding an angle of $0.6 - 0.8 \, \text{rad}$ and $1 - 1.5 \, \text{rad}$ respectively. This discrepancy might be due to the different measurement techniques [13], the difference in growing conditions and/or type of strain used. The big range within both data sets suggests that it might vary among individiual cells. But it is not unlikely that the angle is not fixed, but has a certain degree of freedom. The forces the flagella exert on the cell body change periodically, which could result in a periodically varying angle. The flagella mostly beat in synchrony with slips occuring every $\sim 0.2 \, \text{s}$ or 10 cycles [22], and can be regarded as two coupled oscillators. One of the first observations of this phenomenon was by Huygens in the 17th century [6]. He observed two pendulum clocks, both attached to the same beam. He noticed that within half an hour the clocks were ticking in anit-phase (the phase difference was π), regardless of the initial phase difference. At first he thought the air flow created by the pendula was responsible for this behaviour, but later he realised that the attachment to the same beam provided the necessary coupling. He called this behaviour odd sympathy. The flagella have been modeled as two noisy coupled oscillators [22, 51], where hydrodynamic interactions were used as the coupling mechanism. But similar to the clocks of Huygens, maybe not the medium but the anchoring provides the strongest coupling? The influence of the flexibility of the anchoring in combination with the distal striated fiber is not yet considered in any studies, nor is the coupling through the translation and rotation of the cell body. Hydrodynamics creates a coupling but it is weak and long-ranged. Moreover the theory adresses synchronisation of two cilia a distance d apart, whereas the flagella of *Chlamydomomnas* are connected at their base.

The flagella are connected via the distal striated fiber, see figure 3.3, which contains the protein centrin. The latter forms calcium sensitive, contractile fibers about which the sourcebook notes: *"Several lines of evidence suggest that centrin fibers contract in vivo with changes in calcium concentration.* " The passive influence of the distal striated fiber for synchronisation is an interesting topic for future research. It is not unlikely that active movement of this fiber plays a role in the tumbling events.

3.4 Experimental flows

The flow near a *Chlamydomonas* cell obtained by Drescher et al. [18], see figure 3.4, is an average over several seconds, thereby averaging over several beat cycles and rotations about the swimming axis. It was noticed that the flow can be reproduced by a simple model of three point forces. One located at the center of the cell body, the other two at the 'average' flagellar position. Taking the average over a rotation reproduced the measured fields. Only for $r > 7R$, with R the body radius, the field starts resembling a stresslet field.

For the theoretical squirmer the flow is known exactly, see appendix F. In figure 3.5, flows for different dipole strengths are displayed. The first mode is a pure source doublet term, the leading term in the second mode is a stresslet but the squirmer model does not capture the near field well.

The velocity of a single cell during a stroke with period T is shown in figure 3.6. The effective stroke lasts 60% of the cycle time, where it reaches a top speed of $500 \, \mu\text{m/s}$. At this top speed it creates the strongest flow, similar to the time averaged flow. The flows during the effective and
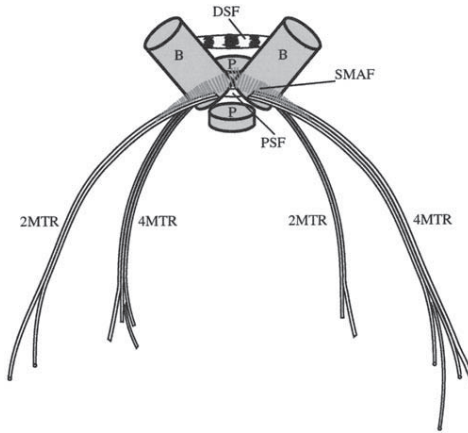
Figure 3.3: The basal parts (bb) of the flagella are attached to the cytoskeleton via four bundles of microtubuli (MTR). The distal striated fiber (DSF) creates a second intra flagellar connection. Taken from [25].

recovery stroke show a strong time-dependence and have been obtained by Guasto et al. [23], see figure 3.10 and 3.11. This highly time-dependent flow field was not yet understood, in the next section I present a simple model which reproduces the flow fields in full detail.

3.5 Three-point-force model

During the beating cycle both the flagella exert a force on the fluid, and the cell body also exerts a force on the fluid. The three-point-force model reduces a *Chlamydomonas* cell to these three forces, see figure 3.7. The magnitude of the force a flagellum exerts is calculated by integrating the force density $\vec{f}$ per unit length of the flagellum:

$$\vec{F}_i = \int_S \vec{f}_i ds_i \ , \ i = 1, 2 \, , \tag{3.1}$$

where s is the distance of a point on the flagellum measured along the flagellum, see figure 3.8. As the cell is force-free ($\sum \vec{F}_i = 0$), the cell body exerts a force $\vec{F}_c = -(\vec{F}_{f,1} + \vec{F}_{f,2})$ on the fluid. Regarding *Chlamydomonas* as a sphere, the force $\vec{F}_c = 6\pi\eta R U \hat{p}$ on the cell body is calculated using the velocity of the cell, see figure 3.6, with $\hat{p}$ the unit vector along the swimming direction. The cell body force is exerted at the center of the cell body, the positions where the flagellar forces are exerted change during the beating cycle. I introduce the flagellar force positions as:

$$s_{f,i} = \frac{\int_S s_i \vec{f} ds_i}{\int_S \vec{f} ds_i} \, , \tag{3.2}$$

whereby the curve S changes during the beating cycle. The force densities can be estimated using video analysis of the stroke, as has been done for spermatozoa [21]. However, I assume
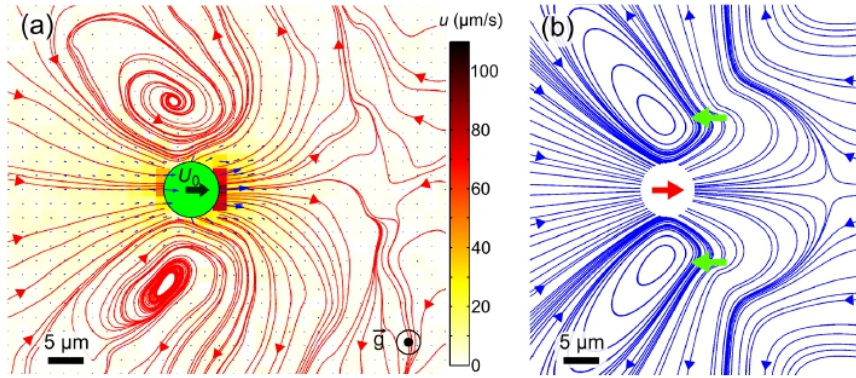
Figure 3.4: Flow field measurements (left) averaged over several seconds and averaged three-point-force model (right). Taken from [55].

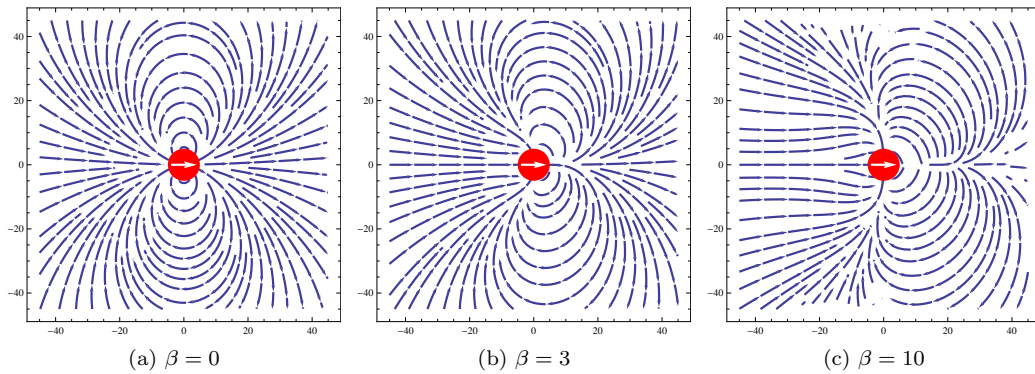(a) $\beta = 0$ (b) $\beta = 3$ (c) $\beta = 10$

Figure 3.5: Squirmer flows for three different ratios of first B_1 and second mode B_2: $\beta = B_2/B_1 > 0$ for a puller type squirmer. The second mode creates a source doublet field in leading order, the first mode is a pure stresslet.
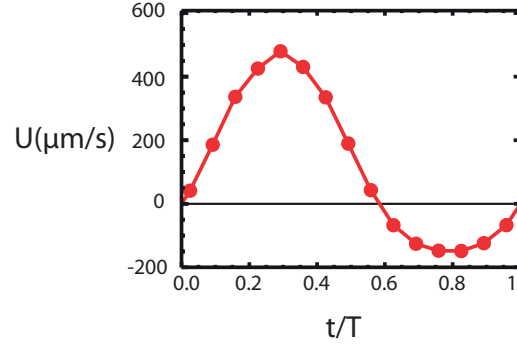
Figure 3.6: The velocity profile of the cell body during a beat cycle ($T = 0.02s$) in a quasi 2D environment. During the effective stroke the cell body moves forwards, during the recovery stroke the cell body moves backwards. Taken from [23].
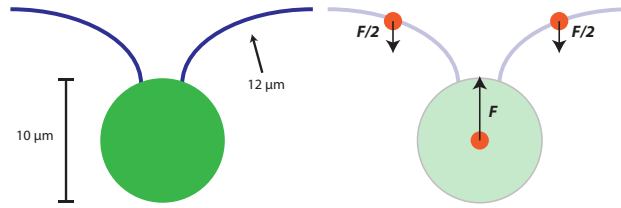
Figure 3.7: Chlamydomonas is modeled as three-point-forces. The flagella both exert a force in equal direction, the cell body exerts a force in the opposite direction of twice the magnitude of a single flagellar force.

the flagellar forces to be of equal strength $\vec{F}_{f,1} = \vec{F}_{f,1} = -\vec{F}_c/2$ and parallel to the swimming direction. During the effective stroke the flagellum moves backward, thus the flagellar forces point backwards. The flagellum is only slightly bent during the effective stroke which leads to an average force position relatively far away from the cell body. At the beginning of the effective stroke the complete flagellum is moving, during the last part of the effective stroke only the distal part moves and continues moving until the flagellum is almost fully stretched backwards. The average force position for the effective stroke moves from the posterior to the anterior side. During the recovery stroke the flagellum is strongly bend, leading to an average force position closer to the cell body. For the recovery stroke the average force position is located at the bend of the flagellum, therefore being only on the posterior side, and not extending as far forwards as the

20

Figure 3.8: Schematic overview of flagellar forces during effective stroke. The distance from the cell body measured along the cell body is s. The flagellum moves backwards, exerting a force density per unit length of flagellum $\vec{f}$ on the fluid.

effective stroke. I assume that the flagellar force position only moves parallel to the swimming direction and makes a jump between the effective and recovery stroke when the speed of the cell body is zero. This leads to a beat cycle as shown in figure 3.9. A single point force exerted at
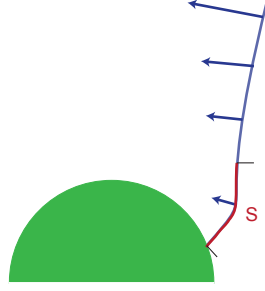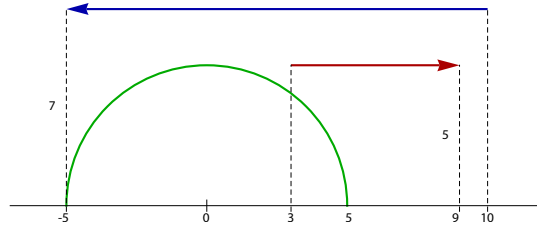

Figure 3.9: The schematic swimming stroke. The point at which the flagellar point force is exerted during the effective stroke (blue) and recovery stroke (red). All distances in μm with the center of the cell body as the origin. the green semi-circle denotes half of the cell body. During the effective stroke the flagellum are almost stretched, thus resulting in a flagellar point force position further away from the cell body compared to the effective stroke in which the flagellum is strongly bent.

the origin creates a stokeslet flow:

$$\vec{u}_{Sto,3D}(\vec{r}) = \mathbf{T}(\vec{r}) \cdot \vec{F} \ , \ \mathbf{T}(\vec{r}) = \frac{1}{8\pi\eta r} \left(\mathbf{I} + \frac{\vec{r} \otimes \vec{r}}{r^2} \right) \ , \tag{3.3}$$

where bold symbols denote tensors, I is the identity matrix. As the Stokes equation is linear, the complete flow is assumed to be a superposition of three stokeslets:

$$\vec{u}(\vec{r}) = \sum_i \mathbf{T}(\vec{r} - \vec{r}_i) \cdot \vec{F}_i \ , \ i = 1, 2, c \ , \tag{3.4}$$

with $\vec{r}_i$ the force positions which change during the beating cycle. In figure 3.10 and 3.11 my calculations are compared to experimentally obtained flows [23]. During the part of the effective stroke, where the flagella are on the posterior side (3.10a-c) two vortices occur at the anterior side of the cell body. When the tips of the flagella are in line with the center of the cell body (3.11d), the dipole field vanishes and a quadrupole-like field occurs. In the last part of the effective stroke,

where the flagella are at the anterior side (3.11e), the two vertices occur on the posterior side of the cell body. For the recovery stroke (3.11f) the field is similar to that of the first part of the effective stroke except for a sign change. The simple 3D model shows good agreement with the experiments. The experiments of Guasto et al. [23] were performed in a thin liquid film bounded by two liquid-air interfaces. The diameter of the cell body of the *Chlamydomonas* used in this experiment was $7 - 10 \, \mu$m and the width of the film $15 \pm 2 \, \mu$m. Only cells where the flagella were beating in a plane parallel to the interfaces were tracked. For soap films with suspended particles a transition occurs between three dimensional and two dimensional behaviour. By comparing the diffusion of particles of size d in a film with a thickness h the self diffusion showed a 2D-3D transition at a ratio $h/d = 7 \pm 3$ [57]. For the *Chlamydomonas* experiments $h/d = 2$, clearly below this empirical limit. In the *Chlamydomonas* thin film experiments it was noted that the far field scaled like $u \sim 1/r$ which is a clear 2D effect, a dipole field in 3D decays like $u \sim 1/r^2$, see appendix C. A two dimensional stokeslet due to a point force exists [56]

$$\vec{u}_{Sto2D}(\vec{r}) = \mathbf{T}(\vec{r}) \cdot \vec{F} \ , \ \mathbf{T}(\vec{r}) = \frac{1}{4\pi\eta} \left(-ln \left(\frac{r}{r_0} \right) \mathbf{I} + \frac{\vec{r} \otimes \vec{r}}{r^2} \right) , \qquad (3.5)$$

where r_0 is a length scale, it is an undetermined constant as there is no typical length scale in an infinite 2D liquid. For a superposition of point forces like in the 3D model the flow is independent of r_0 as long as $\sum_i \vec{F}_i = 0$, see appendix C.

Substituting the 2D Stokeslet in the three-point-force model creates even better agreement with experiments, see figure 3.10 and 3.11. Although the 2D Stokeslet can be deduced mathematically, the physical interpretation is not clear. The 2D problem of a point force is equivalent to an infinitely line in 3D where a constant force density per unit of length is exerted. A solution of the Stokes equation for this problem does not exist, the infinite long line force results in an infinite Reynolds number, regardless of the magnitude of the force density. This is known as the Stokes paradox. Nonetheless using a 3D Stokeslet for a thin film is a gross approximation too, and the 2D stokeslet model shows better agreement. A solution would be to use the 3D stokeslet and incorporate the reflections at the interfaces. Analytic solutions for the flow induced by a point force between two rigid walls exist, but is complex [38]. Simpler approximations exist for a point force near a single wall [7], but they only predict the flow well for relatively large separations, which is not the case for the experimental set-up. Besides, the fluid-air interface is not actually a rigid wall, as only the normal component of the fluid velocity is zero at the interface, which is a strong motivation to describe the system as a 2D fluid.

The time-averaged flow field in figure 3.4 can be obtained by a weighted average of the time dependent three-point-force model, thereby also averaging about a rotation about its swimming direction. The weighting factor is the magnitude of the force obtained from the swimming speed, see figure 3.6.

The simple three point model does not incorporate interactions between the flagella, cell body nor with externally applied flows. A more detailed description of average positions during the beat cycle and taking into account the transverse forces exerted by the flagella might improve the results, but the simple model presented here explains the experiments within experimental errors. Also the flow around the cell body due to the no-slip boundaries is already more complex than a simple Stokeslet, there is a source doublet contribution. But zooming in this much the asphericity and visco elasticity of the cell body might affect the flow field too.

In this chapter I have presented a new hypothesis for the synchronisation of the flagella, it might not be due to the hydrodynamic interactions between the flagella but due to the connection of the flagella both at their base and via the distal striated fiber. Using a schematic analysis of the swimming stroke of *Chlamydomonas* I have presented a simple three-point-force model which reproduces the full details of the highly time dependent swimming induced flow fields, whereby
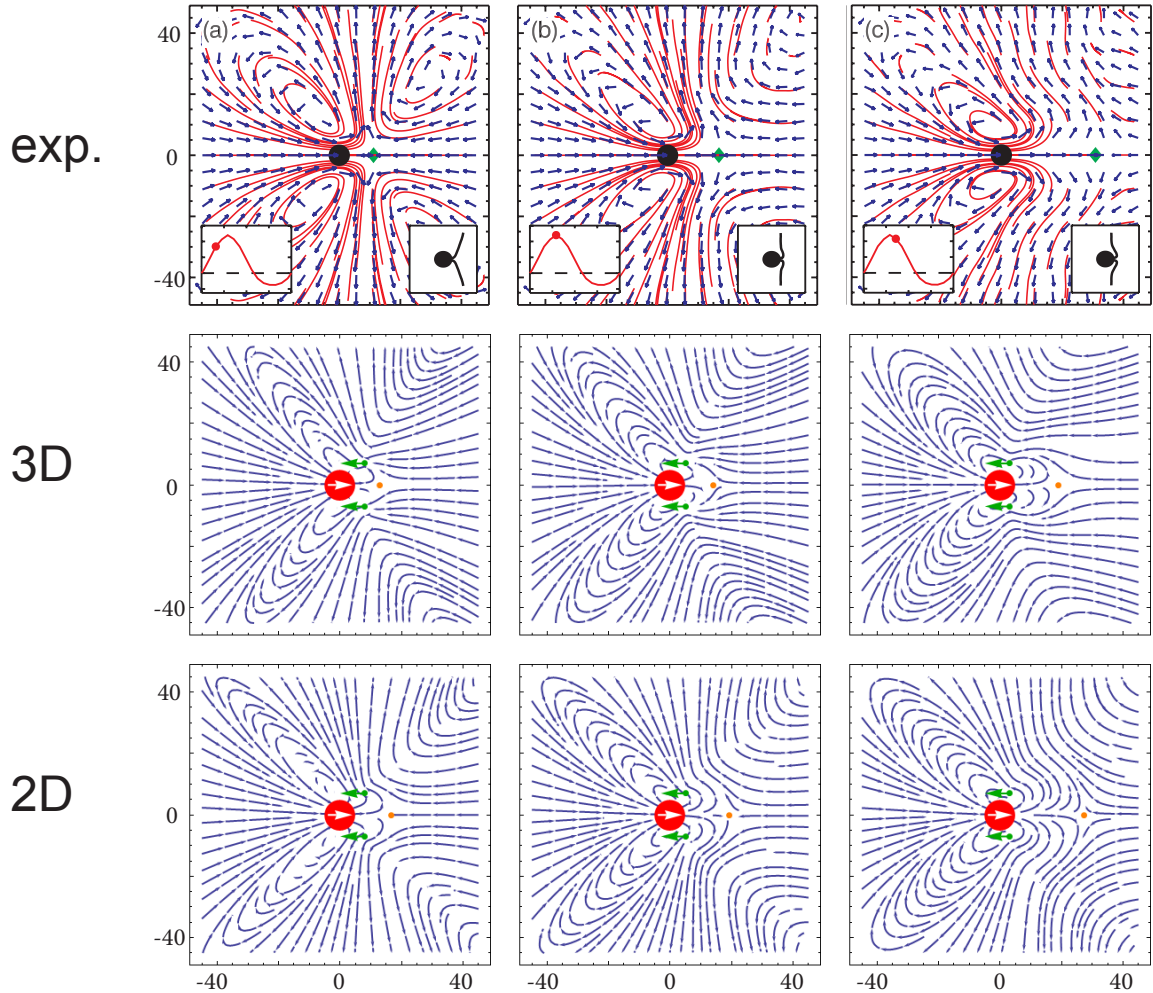
Figure 3.10: The experimental flows during the first half of the beating cycle [23]. The insets show the velocity as a function of time and the flagellar configuration. The second and third row are the analytic flows of three-point-force model using 2D and 3D stokeslets respectively. The green diamond (exp.) and orange dot (3D & 2D) denotes the stagnation point of the fluid, i.e. the point at which the fluid velocity is zero. All lengths are in μm.

the geometry of the experimental set-up is taken into account by modelling the fluid as a 2D liquid.
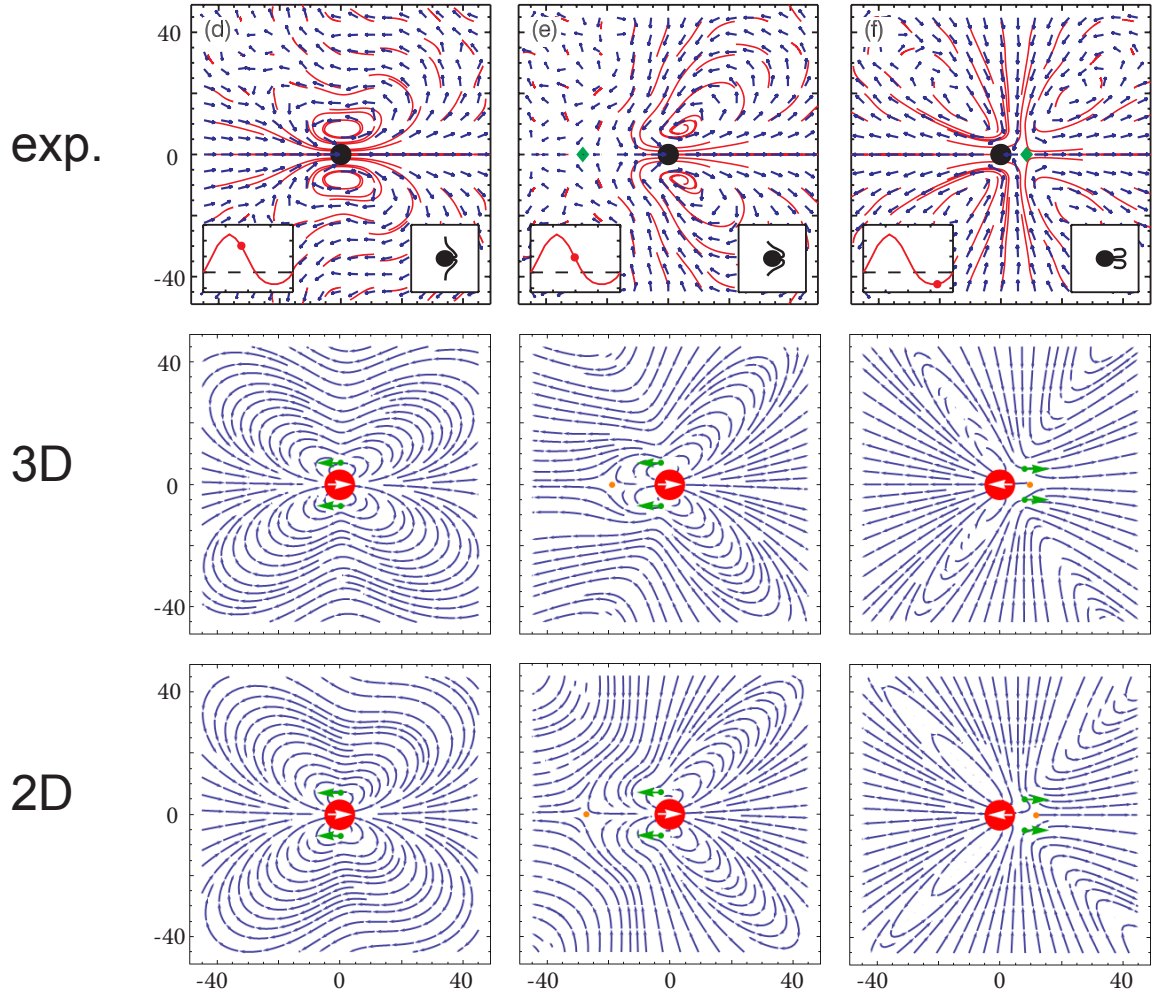
Figure 3.11: The experimental flows during the second half of the beating cycle [23]. The insets show the velocity as a function of time and the flagellar configuration. The second and third row are the analytic flows of three-point-force model using 2D and 3D stokeslets respectively. The green diamond (exp.) and orange dot (3D & 2D) denotes the stagnation point of the fluid, i.e. the point at which the fluid velocity is zero. All lengths are in μm.

Chapter 4

Rheology of a suspension of *Chlamydomonas* Reinhardtii

The previous chapter addressed the swimming motion and induced flows on the micrometer scale, this chapter focuses on the macroscopic influence of swimming of *Chlamydomonas*. After a short introduction of viscosity and the cone-plate rheometer in sections 4.1 & 4.2, I continue with presenting an overview of theory on the effective viscosity of dilute passive suspensions in section 4.3 treating both gravitational and shape effects. In section 4.4 two new derivations are provided for the effect of swimming on the viscosity of dilute suspensions by application of the three-point-force model. The viscosity will turn out to depend on the average swimming direction. A literature study on the latter is presented incorporating both shape and gravity as well as rotary diffusion. A comparison is made between theory and experiments in section 4.6, and numerical results are discussed in 4.7. Finally in section 4.8 non-dilute suspensions are briefly addressed. My contribution consists of two new derivations for the effective viscosity of a suspension of *Chlamydomonas* cells and a review of existing literature on this topic.

4.1 What is viscosity?

The viscosity of a fluid describes the resistance of a fluid to applied shear stresses. Let us consider the experiment of section 2.1 of swimming in molasses. It will be much harder to move your limbs in molasses than in a regular swimming pool filled with water, due to the higher viscosity of molasses. The viscosity is a measure of the microscopic interactions and the momentum transfer at the molecular level. Macroscopically, it relates the strain rate to the stress tensor. For a Newtonian fluid the latter is

$$\boldsymbol{\sigma} = -p\mathbf{I} + 2\eta\mathbf{e}\,, \tag{4.1}$$

with p the pressure, η the viscosity and the strain rate tensor is given by

$$\mathbf{e} = \frac{1}{2}(\nabla\vec{u} + (\nabla\vec{u})^T)\,. \tag{4.2}$$

The area of physics considering the behaviour of complex fluids under shear deformations is called "rheology".
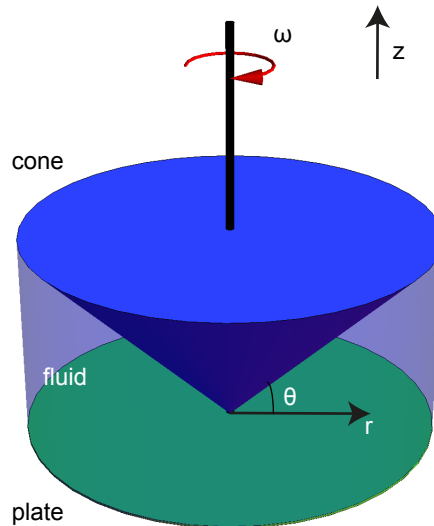
4.2   Cone-plate rheometer and simple shear flow

Figure 4.1: A schematic overview of a cone-plate rheometer.

There exists a variety of viscosity mesurement instruments, but one of the widely used is the cone-plate rheometer. It consists of a flat stationary disk and a downwards pointing, rotatable cone (angle $\theta = 2\,°$) with the same radius. The fluid is located between the cone and the plate, see figure 4.1. The cone rotates with angular velocity ω due to a torque τ. We use a cylindrical coordinate system with the tip of the cone as the origin. The azimuthal velocity at the surface of the cone is $u_\phi = \omega r$. The distance between cone and plate is $h = \tan(\theta)r \sim \theta r$. By solving the Stokes equation (2.2) the fluid velocity is obtained as $(u_r, u_z, u_\phi) = (0, 0, z\omega/\theta)$, and the vorticitiy of the flow is

$$
\begin{aligned}
\nabla \times \vec{u} &= -\frac{\partial u_\phi}{\partial z}\hat{r} + \frac{\partial(r u_\phi)}{r \partial r}\hat{z} \\
&= -\frac{\omega}{\tan\theta}\hat{r} + \frac{z}{r}\frac{\omega}{\tan\theta}\hat{z}\,.
\end{aligned}
\tag{4.3}
$$

The maximum value for $z/r = \tan(\theta) \sim 0.03$, so that the latter term in eq. (4.3) is negligible. Thus in good approximation the flow can be treated as a simple shear flow with constant shear rate $\omega/\tan(\theta)$, which can be created by translating a plate with a velocity U_{plate} relative to a stationary parallel plate, see figure 4.2. Instead of cylindrical coordinates a cartesian coordinate system is used for the simple shear flow, with the axes as shown in figure 4.2. Only the x-component of the flow is nonzero

$$
u_x = \frac{U_{plate}}{H}y = 2e_{xy}y = \dot{\gamma}y\,.
\tag{4.4}
$$

To sustain the fluid motion, a force in the y-direction on the surface with normal in the x direction is exerted per unit area. This is the xy component of the stress tensor: σ_{xy}. The shear
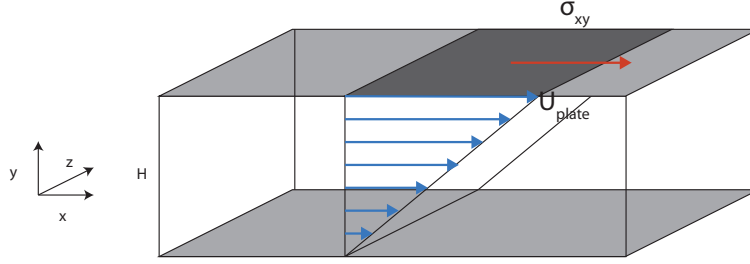
Figure 4.2: A simple shear flow is created by two parallel plates sliding with relative velocity V. The plates are a distance H apart with the fluid in between. To sustain the shear flow a stress σ_{xy} is exerted.

viscosity in the cone-plate rheometer is measured via the relation $\eta = \sigma_{xy}/\dot{\gamma} = \frac{1}{2V}\frac{\tau}{\omega}$. With V the fluid volume in the cone-plate rheometer $V = \tan(\theta)\pi R^3/3 \sim 1ml$. There are $\sim 10^7$ cells in a single experiment for a suspension with a volume fraction $\phi = 1\%$ of suspended cells of size $10\mu m$. The experiments on suspensions of *Chlamydomonas* which are discussed in 4.6 were performed with a cone-plate rheometer as described in this section. In the vicinity of a small particle at position $\vec{r}_0 = (x_0, y_0, z_0)$ the flow can be expanded in a linear, a rotational and a dilatation (or straining) flow, by a Taylor expansion

$$
\begin{aligned}
\vec{u}(\vec{x}) &= \vec{u}_{\vec{x}_0} + \frac{1}{2}(\nabla\vec{u} - (\nabla\vec{u})^T)_{\vec{x}_0} \cdot (\vec{x} - \vec{x}_0) + \frac{1}{2}(\nabla\vec{u} + (\nabla\vec{u})^T)_{\vec{x}_0} \cdot (\vec{x} - \vec{x}_0) \\
&= \vec{u}_{\vec{x}_0} + \vec{\omega}_{\vec{x}_0} \times (\vec{x} - \vec{x}_0) + \mathbf{e}_{\vec{x}_0} \cdot (\vec{x} - \vec{x}_0)
\end{aligned}
\tag{4.5}
$$

with $\vec{\omega}_{\vec{x}_0} = (0, 0, \dot{\gamma}/2)$ and the dilatational tensor

$$
\mathbf{e}_{\vec{x}_0} = \frac{\dot{\gamma}}{2}
\begin{bmatrix}
0 & 1 & 0 \\
1 & 0 & 0 \\
0 & 0 & 0
\end{bmatrix}
= \frac{\dot{\gamma}}{2}\mathbf{R}_{45^\circ}
\begin{bmatrix}
1 & 0 & 0 \\
0 & -1 & 0 \\
0 & 0 & 0
\end{bmatrix},
\tag{4.6}
$$

where $\mathbf{R}_{45^\circ}$ is a rotation matrix, rotating the coordinate frame over an angle 45° about the z-direction. Choosing $Re = 0.1$ as the limit where this expansion is valid, a limiting length scale can be defined. For a volume of size l the typical velocity difference is $\dot{\gamma}l$. The Reynolds number for this volume is: $Re = \rho UL/\eta = \rho\dot{\gamma}l^2/\eta$, susbtituting typical experimental values ($\dot{\gamma} = 5/s$) yields $l \sim 0.14mm$. This is more than an order of magnitude bigger than the size of the cells.

4.3 Rheology of dilute suspensions of passive particles

Chlamydomonas has an almost spherical cell body, therefore I start with the effective viscosity of a suspension of rigid spheres as a first approximation for non-swimming cells. In the following subsections the influence of the gravitiational torque and the asphericity of the cell body are discussed separately.

4.3.1 Spherical particles

For a suspension of rigid spheres Einstein introduced [19, 20] the effective viscosity, which describes a suspension as a homogeneous Newtonian liquid, see figure 4.3. It incorporates the
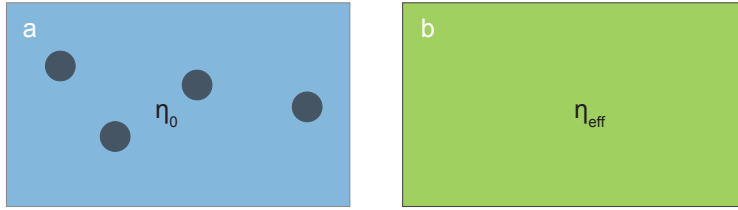
Figure 4.3: The fluid with viscosity η_0 containing many tiny particles (a) is replaced with a homogeneous fluid (b) with an effective viscosity η_{eff}.

viscosity of the suspending medium and the interaction of the suspended particles with the fluid and each other. In the dilute limit particle interactions are negligible, which reduces the many particle problem to a single particle problem of a rigid sphere in an unbounded fluid volume. In appendix G the full derivation of the effective viscosity by Einstein is presented, here I give a brief summary.
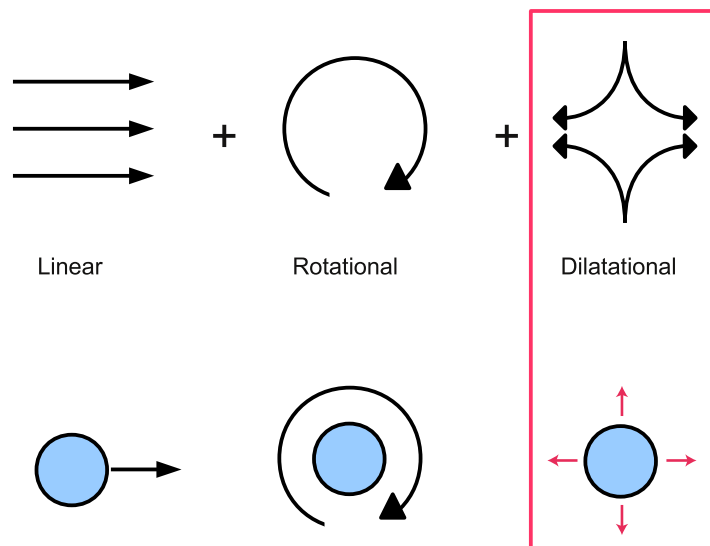
Figure 4.4: (top) Decomposition of an arbitrary flow. (bottom) The behaviour of a rigid sphere in the different flow components.

The Reynolds number in the vicinity of a tiny particle is small ($Re \ll 1$) up to a mesoscopic length scale $L \gg r$, where r is the size of the particle. Within this volume any arbitrary flow can be (Taylor-)expanded, see figure 4.4. The spherical particle instantaneously translates and rotates with the linear and rotational flow. The linear and rotational flows are thus not affected

28
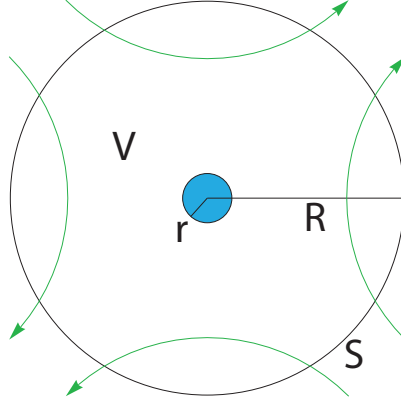
Figure 4.5: A small particle of radius r suspended in a big fluid volume V with radius R bounded by the surface S. The green lines depict the dilatational flow.

by the presence of the particle. The dilatational flow does not exert a net force nor a torque on the sphere, but the particle does reflect the dilatational flow as we demonstrate now. Without loss of generality the calculations are restricted to a pure dilatational or straining flow. We choose a coordinate system with the center of the sphere as the origin, the three axes are parallel to the dilatational axes. In the absence of a particle the undisturbed dilatational flow $\vec{u}_0$ is described by

$$\vec{u}_0 = \mathbf{e}_0 \cdot \vec{r}, \tag{4.7}$$

with the strain rate tensor

$$\mathbf{e}_0 = \begin{bmatrix} A & 0 & 0 \\ 0 & B & 0 \\ 0 & 0 & C \end{bmatrix}. \tag{4.8}$$

Suspending a small rigid sphere disturbs the flow field in the vicinity of the particle. Solving the Stokes equation (2.2) for a small rigid sphere with no slip boundary conditions and the fluid flow at infinity given by eq. (4.7) yields the disturbance flow [19]

$$\vec{u}_1 = -\frac{5}{2} \left(\frac{a^3}{r^3} - \frac{a^5}{r^5} \right) \frac{\vec{r} \cdot (\mathbf{e}_0 \cdot \vec{r})}{r^2} \vec{r} - \frac{a^5}{r^5} \mathbf{e}_0 \cdot \vec{r}. \tag{4.9}$$

The total field outside the particle is then a superposition

$$\vec{u} = \vec{u}_0 + \vec{u}_1. \tag{4.10}$$

Let us consider a concentric sphere with a radius $R \gg r$ of volume V, see figure 4.5. The work done on the outside of this large sphere, to sustain the fluid motion is

$$W = \int \vec{u} \cdot (\boldsymbol{\sigma} \cdot \hat{n}) dS = 2\eta_0 \left(1 + \frac{5}{2}\phi \right) \mathbf{e} : \mathbf{e}, \tag{4.11}$$

where S is the surface boundary of the volume V and $\hat{n}$ the surface normal and $(\boldsymbol{\sigma} \cdot \hat{n})$ is the force exerted on the surface. The double dot product of two tensors is defined as $\mathbf{a} : \mathbf{b} = \sum_{i,j} a_{ij} b_{ij}$. The first term in (4.11) occurs too in the absence of the suspended particle, the $\frac{5}{2}\phi$ part is due

to the presence of the particle. The suspension can now be described as a Newtonian fluid with an effective viscosity

$$\eta_{eff} = \left(1 + \frac{5}{2}\phi\right)\eta_0. \qquad (4.12)$$

The effective viscosity of a suspension is higher than that of the intrinsic medium. In the case of suspensions of passive particles, as considered here, the work done on the outer sphere is equal to the dissipated energy in the volume V. The dilute regime, where this expression is valid and where particle interactions are negligible is $\phi < 2\%$ [4, 41]. The semi dilute regime is defined as $2\% < \phi < 25\%$ where terms in ϕ^2 become relevant. For small shear rates the spherical cell body is not expected to deform, therefore a suspension of passive *Chlamydomonas* is expected to behave like a suspension of rigid spheres. In the rest of this document the viscosity is denoted as $\eta_{eff} = (1 + B\phi)\eta_0$, for rigid spheres $B = 5/2$. The effective viscosity in the dilute limit was first derived by Einstein, it is a function only of the intrinsic viscosity of the suspending medium and the volume fraction of suspended particles.

4.3.2 Gyrotactic particles
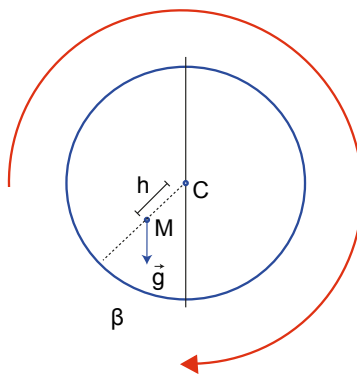
Figure 4.6: A spherical particle with the center of mass (M) and geometric center (C) a distance h apart in an ambient flow with a vorticity ω (red arrow). For small shear rates the line joining the geometrical center and center of mass makes a constant angle β with gravity.

Gravity exerts a force on *Chlamydomonas*, with their density excess over water being 5%. The sedimentation velocity is about $\sim 2\mu m/s$ which is negligible compared to their swimming speed $(40 - 200\mu m/s)$. The mass within the *Chlamydomonas* cell is not homogeneously distributed, the cells are bottom heavy. Gravity exerts a torque on the cell, which is not negligible. It can be employed to create hydrodynamic focusing [39] in a cylindrical channel. The maximum gravitational torque for a spherical particle with a center of mass offset h is $\tau_g = 4/3\pi\Delta\rho a^3 hg$, and the maximum viscous torque a fluid rotating with vorticity ω can exert on a sphere is: $\tau_f = 8\pi\eta a^3\omega$. The ratio of these torques is

$$\lambda = \frac{\tau_g}{\tau_f} = \frac{\Delta\rho gh}{6\eta\omega} \, . \tag{4.13}$$

Brenner [9] derived an effective viscosity for spherical gyrotactic particles as a function of this ratio in the absence of rotary diffusion

$$\frac{\eta_{eff}}{\eta_0} = 1 + \underbrace{(5/2 + 3/2 \sin^2 \theta_s(\lambda))}_{B} \phi \, , \tag{4.14}$$

with

$$\sin \theta_s(\lambda) = \sqrt{\frac{1}{2}(1 + \lambda^2) - \sqrt{\frac{1}{4}(1 + \lambda^2)^2 - \lambda^2 \sin^2 \alpha}} \, , \tag{4.15}$$

where α is the angle between the vorticity vector and gravity. B of eq. (4.14) is plotted in figure 4.7 as a function of the dimensionless, inverse shear rate λ and as a function of the shear rate using *Chlamydomonas* specific values for the parameters. If gravity and vorticity are parallel, then the gravitational torque has no effect on the effective viscosity and the Einstein formula (4.12) is obtained. Here I consider the case that the angle between vorticity and gravity is $\alpha = \pi/2$ and $\sin \alpha = 1$, like in a cone-plate rheometer.
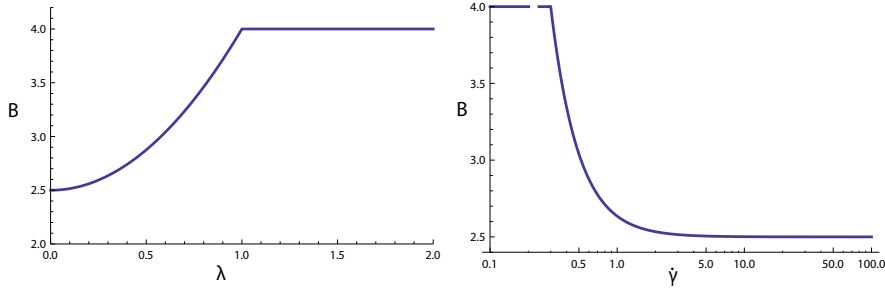
Figure 4.7: (left) Linear viscosity constant as a function of non-dimensionalised gravitational torque. (right) Linear viscosity constant as a function of shear rate using *Chlamydomonas* specific parameters from [5] & [54]. Gravity is perpendicular to the vorticity of the flow $\alpha = \pi/2$).

At small shear rates $\lambda > 1$ the gravitational torque balances the viscous torque, see figure 4.6. The particles do not rotate at all, the line joining the center of mass and the geometric center makes a constant angle with gravity (β). In this limit eq. (4.14) becomes $B = 5/2 + 3/2$. The first part is due to the reflection of the dilatational field, the $3/2$ is due to the reflection of the rotational field. At higher shear rates $\lambda < 1$, the gravitational torque is too small to balance the viscous torque, and the particles start to rotate with the ambient fluid. For high shear rates $\lambda \ll 1$ the gravitational torque becomes negligible compared to the viscous torque and the Einstein result eq. (4.12) is obtained.

In this case the (effective) diffusion is neglected. It will turn out that compared to the effective rotary difussion of swimmin suspension the gravitational effect becomes negligible.

31
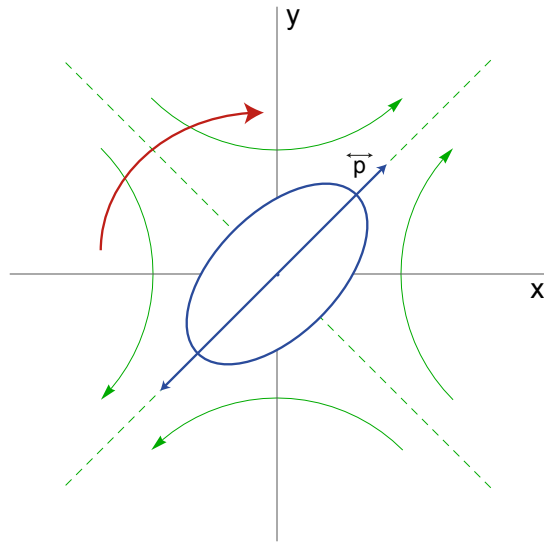
Figure 4.8: An ellipsoid oriented in the plane of shear. The shear flow is decomposed in the dilatational flow (green) and the vorticity (red). In the absence of vorticity the ellipsoid would align along the major dilatational axis, as depicted in this figure.
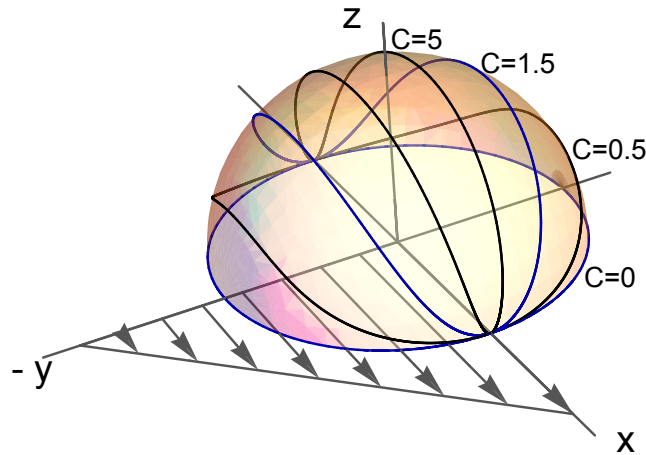
Figure 4.9: Jeffery orbits for several orbit constants C for a prolate spheroid with aspect ratio $\kappa = 10$, induced by a shear flow in the xy-plane.

4.3.3 Ellipsoidal particles

Although *Chlamydomonas* has an almost spherical cell body, it is best described as a prolate spheroid with aspect ratio $\kappa \sim 1.3$. The motion of small ellipsoidal particles in a fluid was addressed by Jeffery [36] in 1922. Similar to Einstein he expanded an arbitrary flow into a
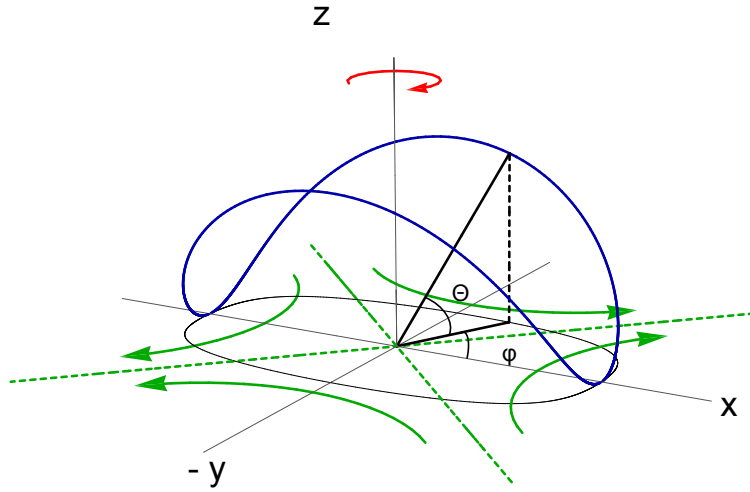
Figure 4.10: The angles ϕ and θ for the spherical reference frame of the particle. The straining flow with the two dilatational axes (green lines), and the vorticity (red arrow).
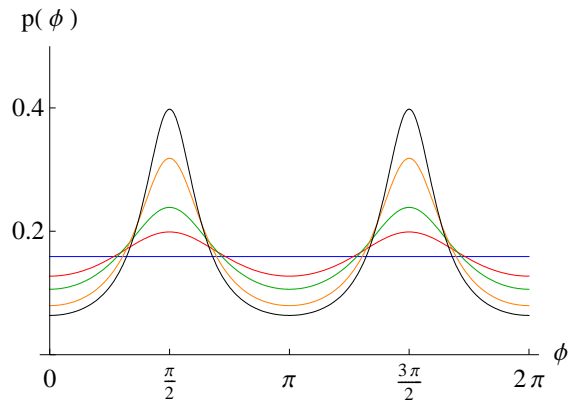
Figure 4.11: Normalised probability density as a function of the azimuthal angle ϕ. For aspect ratios $\kappa = 1$(blue), 1.25(red), 1.5(green), 2(orange), 2.5(black).

rotational, translational and dilatational component. The linear and rotational part of the flows again cause an instant translation and rotation of the particle, but the dilatational flow now exerts a torque depending on the orientation too. The anisotropy of the particle allows us to define an orientation $\hat{p}$ of the particle along the major axis. Instead of simply rotating with the fluid, the particle performs a closed Jeffery orbit. Several orbits for different orbit numbers C are shown in figure 4.9. We use a spherical coordinate system as depicted in figure 4.10 to parametrise the orbit. The angle θ is given by [49]

33

$$\tan(\theta) = \frac{C\kappa}{\sqrt{\kappa^2 \cos^2 \phi + \sin^2 \phi}} \,, \tag{4.16}$$

with C the orbit constant, defined by the initial orientation of the particle. The angular velocity of the azimuthal angle, measured in the plane of shear, is

$$\dot{\phi} = \frac{\dot{\gamma}}{\kappa^2 + 1} \left(\kappa^2 \cos^2 \phi + \sin^2 \phi\right) \,. \tag{4.17}$$

Integrating the latter yields a period of rotation

$$T = \frac{2\pi}{\dot{\gamma}} \left(\kappa + 1/\kappa\right) \,. \tag{4.18}$$

The probability of finding a particle with an angle ϕ is inversely proportional to the angular velocity: $p(\phi) = 1/(T\dot{\phi})$. For the deterministic case the probability density for several aspect ratios is given in figure 4.11. Note that due to the fore-aft symmetry of an ellipsoid the probability density function is π periodic. The combination of dilatational flow and vorticity creates an average value $\langle \phi \rangle = \pi/2, 3\pi/2$. In the absence of vorticity an ellipsoid aligns as depicted in figure 4.8 along one of the dilatational axis. The linear constant B has a lower bound for all aspect ratios, the upper bound diverges for infinite aspect ratios: $2 < B < \infty$ [36].
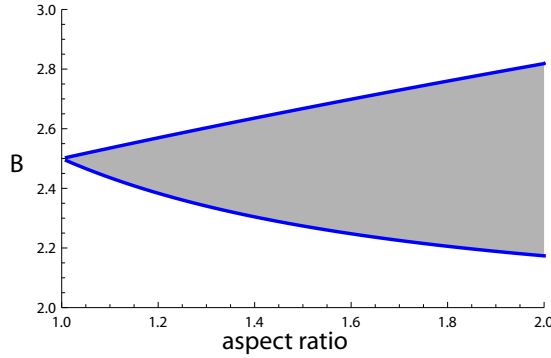
Figure 4.12: Linear viscosity constant as a function of aspect ratio for prolate sheroids. The lower limit corresponds with the ellipsoids being aligned along the z-axis. The upper limit is for particles oriented perpendicular to the z-axis.

An ellipsoid oriented in the z direction rotates with the surrounding fluid and will only distort the dilatational flow. The reflected field is less than for a sphere with the same volume, this corresponds to the lower limit of B. A sphere oriented in the xy-plane has an angular velocity which differs from the vorticity of the flow, thereby not only distorting the dilatational part but also the rotational part of the flow, corresponding to the upper limit of B. Every axisymmetric, and fore-aft symmetric particle performs a Jeffery orbit as if it were a spheroid with an effective aspect ratio [10]. The asphericity of the cell body of *Chlamydomonas* creates a viscosity range which only slightly differs from that of spheres, see figure 4.12. The flagella of *Chlamydomonas* might create a higher effective aspect ratio, but for passive particles this effect will be small, as the cells were observed to rotate uniformly with the flow [59]. Swimming cells behave differently, they align for two third of the time in the x-direction and rotate for the other one third of time. For an ellipsoid I define

$$\tau = \frac{t(\phi = \frac{\pi}{4} \to \frac{3\pi}{4})}{t(\phi = \frac{3\pi}{4} \to \frac{5\pi}{4})} \tag{4.19}$$

as the ratio of alignment time and tumbling time, where ϕ denotes the angle as in eq. 4.17.

$$\tau = \frac{\pi - 2\mathrm{ArcCot}(\kappa)}{2\mathrm{ArcCot}(\kappa)}. \tag{4.20}$$

The experimental value $\tau \sim 2$ corresponds to an effective aspect ratio $\kappa_e = 1.7$. In section 4.4.2 the theoretical work of Jones et al. [37] is discussed who showed that the beating flagella in combination with a spherical cell body creates an effective ratio of $\kappa_e = 1.1$. The actual value of B depends on the average orientation of the particles, this is addressed in section 4.5. The aspherical cell body of *Chlamydomonas* creates a small deviation in the effective viscosity compared to perfect spheres: $B = 2.5 \pm 0.1$, the effective aspect ratio of swimming cells creates a slightly bigger deviation: $B = 2.5 \pm 0.3$. The shape of the particle has a small effect on the effective viscosity, which depends on the average orientation of the particles. The latter is addressed in section 4.5.

Based on the separate analysis of the influence of asphericity and gravity, the viscosity of a suspension of non-swimming *Chlamydomonas* is best described as the viscosity of a suspension of rigid spheres. At small shear rates ($\lambda \gg 0$) gravity enhances the viscosity.

4.4 Rheology of dilute suspensions of swimming *Chlamydomonas*

In this section I present two new derivations of the influence of swimming of *Chlamydomonas* on the effective viscosity of the suspension.

4.4.1 Three-point-force model

Chlamydomonas has an almost spherical cell body, which serves as a motivation to model it as a rigid spherical particle with radius a which creates an additional flow due to swimming. Recall that the latter is described by a superposition of three stokeslets, see eq. (3.3). Using the same approach as in section 4.3 for passive spheres, the work done on the surface of a large spherical volume containing the particle is compared to the same fluid volume containing a homogeneous fluid. This volume is large compared to the size of the particle. A surface integral over this volume or a volume average will not depend on the near field, but rather on the far field behaviour. Here a brief summary of the derivation of the effective viscosity is given, the full derivation is provided in appendix G. By substituting the multipole expansion

$$\frac{1}{|\vec{r} - \vec{r}_1|} = \frac{1}{r} + \frac{\vec{r}_1 \cdot \vec{r}}{r^3} + O(r^{-5}). \tag{4.21}$$

in equation (3.4) the far field is obtained as (see appendix D)

$$\vec{u}_s = -\frac{3}{8\pi\eta} \hat{r} \frac{\mathbf{S} : (\hat{r} \otimes \hat{r})}{r^2}. \tag{4.22}$$

with the stresslet tensor being

$$\mathbf{S} = S\left(\hat{p} \otimes \hat{p} - \mathbf{I}/3\right), \tag{4.23}$$

where $\hat{p}$ denotes the swimming direction of the cell. The stresslet strength $S = \frac{bF}{2}$ depends on position and magnitude of the point forces, see figure 4.13, and it changes during the swimming stroke. During the major part of the stroke *Chlamydomonas* is a puller ($S > 0$), for the minor part of the effective stroke, where the effective flagellar forces are behind the centerline of the cell body, it is a pusher ($S < 0$). As viscosity experiments typically last several seconds, the stresslet strength denotes the average over a beat cyce $S = \langle S \rangle_t$. The magnitude of S can be derived from the flows and swimming speed. The positions of the point forces in the flows of figure 3.4 provide the dipole length b. With the linear relation between force and velocity for low Reynolds numbers and considering the cell as a sphere with radius a, the dipole force is calculated from $F = 6\pi\eta a \langle U \rangle$. Throughout this chapter a value $\langle U \rangle = 40\,\mu\text{m/s}$ is used [59]. The total flow is a superposition of the applied flow, the reflected flow and the swimming induced flow:

$$\vec{u} = \vec{u}_0 + \vec{u}_1 + \vec{u}_s. \tag{4.24}$$

Evaluating the work done on a big sphere containing the microswimmer in order to sustain the motion (G.5) yields

$$\frac{W}{V\eta_0} = \left(1 + \frac{5}{2}\phi\right)\mathbf{e} : \mathbf{e} + \frac{n}{V}\mathbf{S} : \mathbf{e}. \tag{4.25}$$

with n the number density of swimmers. By substituting $S = bF/2 = 3b\pi\eta rU$ this is recast as

$$\frac{W}{V\eta_0} = \left(1 + \frac{5}{2}\phi\right)\mathbf{e} : \mathbf{e} + \frac{9}{4}\phi\frac{b}{a}\frac{U}{a}(<\hat{p}\otimes\hat{p}> - \mathbf{I}/3) : \mathbf{e}. \tag{4.26}$$

where $\langle ... \rangle$ denotes the ensemble average over both particle orientation and time and ϕ is the volume fraction of suspended particles. The $\otimes$ symbol denotes the dyadic, tensor or Kronecker product. In this case the work done on the outer sphere is not equal to the dissipated energy within the fluid volume. The dissipation in the system is given by eq. (4.25) with an additional term $\sim \mathbf{S} : \mathbf{S}$. The the cell metabolism leads to a dissipation too, but it is not taken into account here. The liquid crystal order parameter $\mathbf{Q} = \langle\hat{p}\otimes\hat{p}\rangle - \mathbf{I}/3$ is used in the rest of the document. A cone-plate rheometer measures the viscosity as $\eta = \sigma_{xy}/e_{xy}$. The effective viscosity is given by

$$\frac{\eta_{eff}}{\eta_0} = 1 + \frac{5}{2}\phi + \frac{9}{4}\phi\frac{b}{a}\frac{U}{a\dot{\gamma}}Q_{xy}, \tag{4.27}$$

where is used that $e_{xy} = \dot{\gamma}/2$, see eq. (4.6). This is in agreement with literature[54]. The disadvantage of this derivation is that it is mathematically laborious. It does not provide any new information therefore it is better to use a volume average approach. Using the volume average approach of Landau and Lifschitz [41] another new derivation of the effective viscosity of a suspension of *Chlamydomonas* is derived. The full derivation is presented in appendix H, here again a brief summary. The stress tensor is averaged over a large volume

$$\langle \boldsymbol{\sigma} \rangle = \frac{1}{V}\int \boldsymbol{\sigma} dV, \tag{4.28}$$

which is decomposed in a pressure, strain and particle dependent term as

$$\langle \boldsymbol{\sigma} \rangle = -\langle p \rangle\mathbf{I} + 2\eta_0\langle\mathbf{e}\rangle + n\langle\mathbf{S}_{particle}\rangle, \tag{4.29}$$

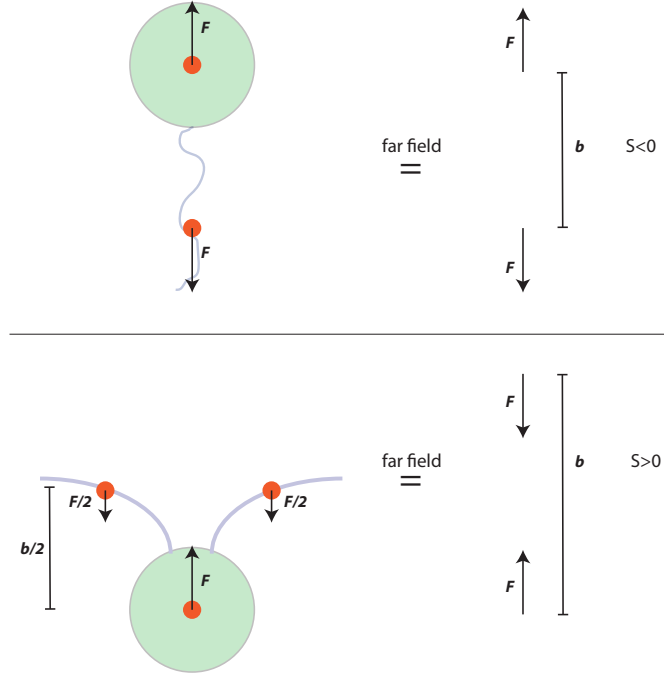Figure 4.13: Top: Spermatozoa generate their thrust at the back of their body inducing a pusher type stresslet $S < 0$. Bottom: The far field of *Chlamydomonas* is a puller stresslet with $S > 0$, the dipole length is twice that of the distance between the flagellar and cell body point forces measured along the swimming direction.

the latter term is recast as a surface integral using Gauss theorem

$$\langle \mathbf{S}_{particle} \rangle = \int \left((\boldsymbol{\sigma} \otimes \vec{r}) \cdot \hat{n} - \eta (\vec{u} \otimes \hat{n} + \hat{n} \otimes \vec{u}) \right) dS \,. \tag{4.30}$$

By substituting in eq. (4.22) the particle stress tensor due to swimming is deduced

$$\langle \mathbf{S}_{sparticle} \rangle = \frac{1}{V} \mathbf{S} \,. \tag{4.31}$$

Combining with the passive result for a sphere, and multiplying with the number density n, one obtains the same result as eq. (4.27). It is the same result as obtained by Batchelor [3], who showed that the stress tensor for a dipole field is: $\boldsymbol{\sigma}_a = \mathbf{S}/V$, and was along different lines obtained by Haines et al. [24] and Simha et al. [63].

Now we discuss the result: the first two terms in eq. (4.27) are the intrinsic viscosity and the passive contribution for spheres, respectively, the last term is the contribution due to swimming. It depends on the non-dimensionalised dipole length $b/a \sim 3$ (obtained from figure 3.4), the volume fraction of suspended particles and the swimming speed. The latter is non-dimensionalised with the velocity difference $(a\dot{\gamma})$ the particle observes due to the shear flow. The viscosity is not a scalar but rather a tensor, the measurement device defines which element of the tensor is measured. Without a detailed understanding of the orientation of the particles, qualitative conclusions can be drawn about the effective viscosity of active suspensions. Therefore, I write the viscosity as a sum over the intrinsic, passive and active contributions

37

$$\eta_{eff} = \eta_0 + \eta_p + \eta_a . \tag{4.32}$$

The passive contribution is independent of shear rate, whereas the active contribution decays with the inverse of the shear rate, see figure 4.14. Thus, for small shear rates the active contribution dominates, for high shear rates the passive behaviour dominates ($\eta_a \simeq 0$).

For small shear rates $\dot{\gamma} < \frac{9bU}{20a^2}$, the effective viscosity can even be smaller than the intrinsic viscosity ($-\eta_a > \eta_p$). For an isotropic distribution of swimming directions $Q_{xy} = 0$ and $\eta_a = 0$, thus an anisotropic distribution is necessary for swimming to contribute to the viscosity. In figure 4.15 two limiting cases for the swimmer, one for which $Q_{xy} = 1/2$ and one for which $Q_{xy} = -1/2$. In the first case a maximum increase in the effective viscosity is achieved, in the latter case a maximum decrease in the effective viscosity is achieved.
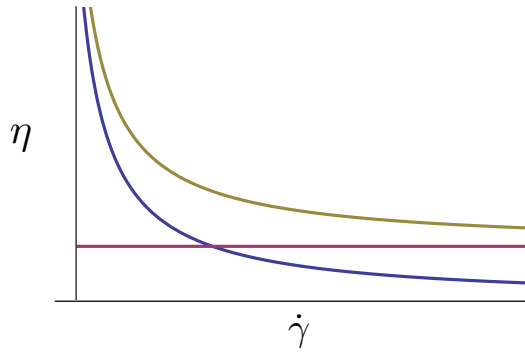

Figure 4.14: The effective passive viscosity η_p (red), the effective active viscosity assuming a constant $Q_{xy} > 0$ (blue) and the sum $\eta_p + \eta_a$ (yellow).

The far field of a force-free swimming object is that of a dipole of strength S. The sign determines whether the microswimmer is a puller ($S > 0$) like *Chlamydomonas* or a pusher ($S < 0$). The dipole creates an orientation-dependent contribution to the stress tensor called the stresslet which can be both positive and negative, resulting in an increase or decrease of the effective viscosity.

4.4.2 Incorporating flagella

Using resistive force theory Jones et al. [37] studied the effect of the flagella for *Chlamydomonas*. The cell body was modeled as a rigid sphere, reflecting the external flow. Using a simple effective and recovery stroke they reproduced the swimming speed well. Although the flagella are highly anisotropic, the torque exerted by the straining flow via the flagella on the cell body is small compared to the torque exerted by the rotational flow. According to the model of Jones et al. the spherical cell body in combination with the beating flagella leads to an effective aspect ratio $r \sim 1.1$ [37]. The visual microscopic observations of Pedley [54] showed that the cells in their experiments were best described as an ellipsoid with an aspect ratio of $\kappa = 1.38$.

The flagella of *Chlamydomonas* only slightly influence the effective viscosity, as they create a small effective ratio. The major contribution of the swimming movement to the effective viscosity is due to the induced flow field. Thus swimming of *Chlamydomonas* can both increase
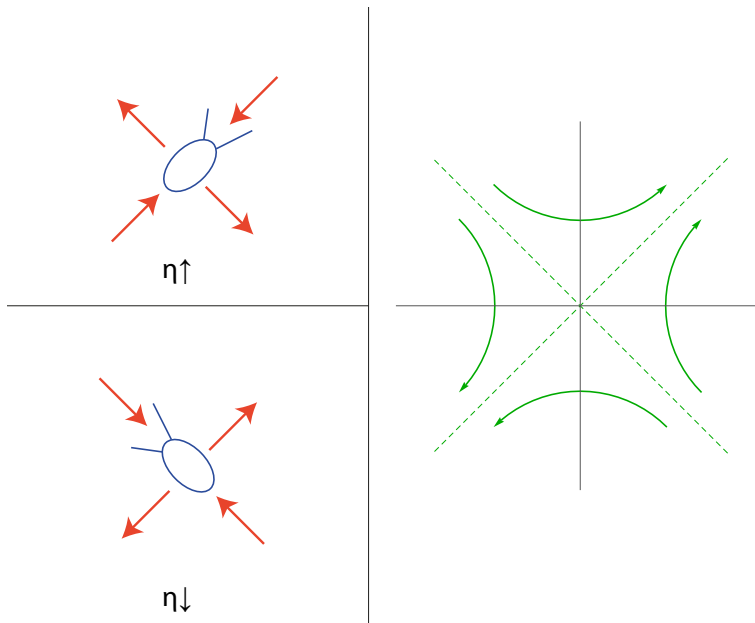
Figure 4.15: Right: the dilatational part of the shear flow. Left upper: a swimming *Chlamydomonas* cell enhances the viscosity. Left lower: a swimming *Chlamydomonas* cell decreases the viscosity.

or decrease the effective viscosity depending on the average orientation of the cells, the latter will be addressed in the next section.

4.5 Statistical description

In this section I present my literature study on the statistical description of a suspension of many cells. The experimental volume in a cone-plate rheometer contains 10^7 particles. This high number allows us to describe orientation of the particles with the probability density function $\psi(\hat{p})$, which obeys the Fokker-Planck equation

$$D_r \nabla^2 \psi - \nabla \cdot (\dot{p}\psi) = 0 \,, \tag{4.33}$$

whereby ∇ the gradient operator over the surface of the unit sphere, and D_r is the rotational diffusion constant. In the second term the deterministic rate of change of the orientation $\dot{p}$ is given as [54]

$$\dot{p} = (\mathbf{I} - \hat{p} \otimes \hat{p}) \cdot (\beta \mathbf{e} + \mathbf{W}) \cdot \hat{p} + B_g^{-1}(\mathbf{I} - \hat{p} \otimes \hat{p})\hat{k} \,. \tag{4.34}$$

The first part is the Jeffery orbit, with $\beta = (\kappa^2 - 1)/(\kappa^2 + 1)$ depending on aspect ratio, the latter part is due to the gravitational couple, with gravity acting in the $-\hat{k}$ direction. $B_g = \frac{\eta_0 \alpha_\perp}{2h\rho g}$ is the gyrotactic orientation time, with $\alpha_\perp \simeq 1.08$. For particles with an homogeneous mass distribution the latter term is omitted. Particle interactions are not taken into account, thereby restricting the validity to the dilute limit $\phi < 2\%$. The active swimming is either introduced as an effective higher rotational diffusion, or by modeling tumbling as a Poisson process [62]. For ellipsoidal swimmers in general, distribution functions have been obtained for infinitely long,
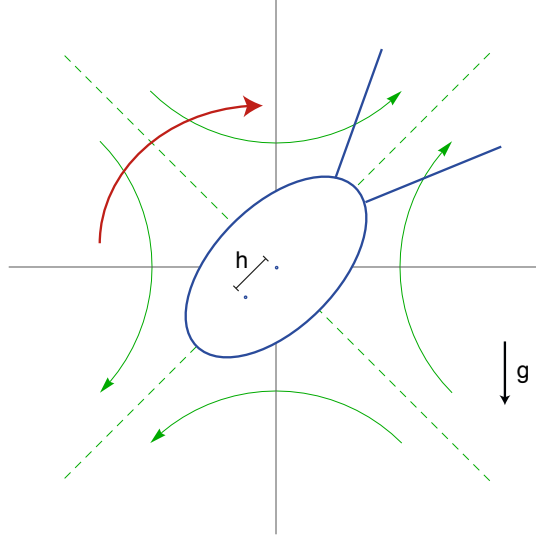
Figure 4.16: A bottom-heavy *Chlamydomonas* cell with an ellipsoidal cell body with a center of mass offset h.

non-gyrotactic tumbling rods [62], for non gyrotactic, high aspect ratio particles applying liquid crystal theory [27], for non-gyrotactic ellipsoids by introducing white noise in the orientation of the force dipole [24], etc. The general result is $1/2 > Q_{xy} > 0$ for ellipsoidal particles. This leads to an increase of the viscosity due to swimming for elongated pullers and a decrease for elongated pushers. In the absence of rotary diffusion and gravity the particles perform a Jeffery orbit, yielding a probability density function as in figure 4.11, which is symmetric in $\phi = \pi/2$. Rotary diffusion does not only flatten this distribution but also skews it. This is illustrated with a small Gedanken experiment of two ellipsoidal particles. They rotate in the $+\phi$ direction and at a certain time are at an angle $\phi = \pi/2$. At that instant rotary diffusion rotates the particles by $\delta\phi$ and $-\delta\phi$ respectively. Also, symmetrically distributed about $\pi/2$. The initial angular velocity after randomisation of both particles is the same, but for $\phi < \pi/2$ the velocity will decrease during a timestep δt, and the velocity of the other particle will increase. For our system of two particles the (unnormalised) probability density for the timestep δt is given by the red shaded areas, in figure 4.17. It is not symmetric about $\pi/2$ like the initial distribution. Many of these randomisation processes skew the probability density function in the $\phi < \pi/2$ direction.

In the absence of gravity eq. (4.34) reduces to

$$\dot{p} = (\mathbf{I} - \hat{p} \otimes \hat{p}) \cdot (\beta\mathbf{e} + \mathbf{W}) \cdot \hat{p}. \tag{4.35}$$

Hinch and Leal [29] solved eq. (4.33) with eq. (4.35) for almost spherical particles. This result was used by Haines et al. [24] to calculate the effective viscosity in the first order of the particle aspect ratio ϵ

$$\frac{\eta_{eff}}{\eta_0} = 1 + \frac{5}{2}\phi + \frac{9}{4}\frac{b}{a}\frac{U}{a\dot{\gamma}}\phi \cdot \underbrace{\frac{1}{5}\frac{\zeta}{1+\zeta^2}}_{Q_{xy}} \kappa N(\kappa), \tag{4.36}$$

with $\zeta = \dot{\gamma}/(6D_r)$ the non-dimensionalised shear rate, κ the aspect ratio and $N(\epsilon) \simeq 0.5$ a
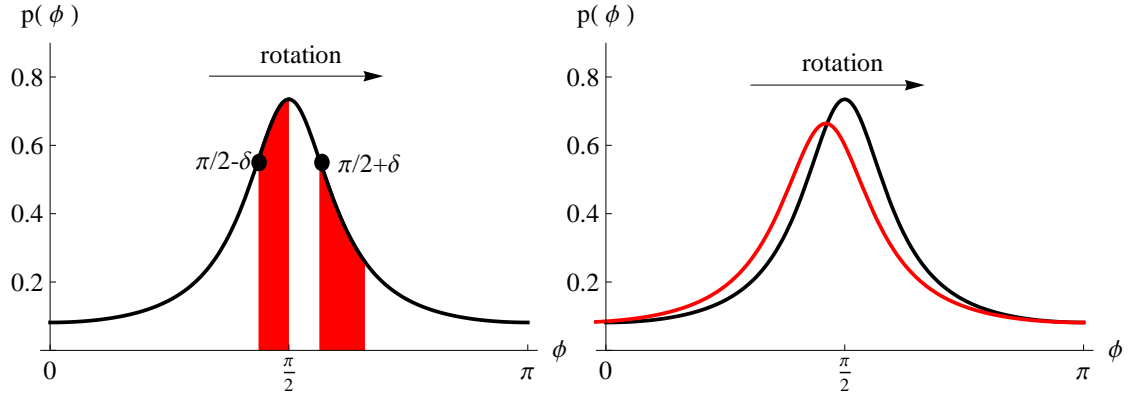
Figure 4.17: Left: Deterministc probability density for a prolate spheroid (black line). The red area is the not normalised probability density function of two particles. Right: Deterministic probability density for a prolate spheroid (black line) and the probability density incorporating rotary diffusion.

geometric function. An aspect ratio $r = 1.3$ is used throughout this section. The average orientation of the particles is due to competition between the applied flow and rotary diffusion. In figure 4.18 eq. (4.36) is plotted using both the passive $D_r = 0.001/s$ and two values for the active rotary diffusion $D_r = 0.4/s$ [35] & $D_r = 0.13/s$ [54]. For $\dot{\gamma} > \dot{\gamma}_c$ the passive contribution dominates, for lower shear rates the viscosity is enhanced, reaching a plateau for small shear rates. $\dot{\gamma} < D_r$. The zero shear rate limit for the active part of the viscosity is $\lim_{\dot{\gamma} \to 0} \eta_a/\eta_0 \sim \frac{U}{aD_r}$
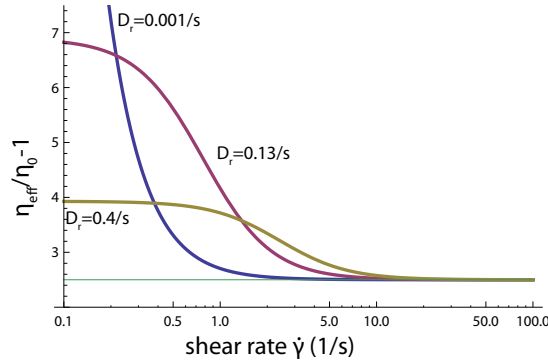
Figure 4.18: The effective viscosity as a function of shear rate in a log-linear plot for three values of the rotary diffusion constant and the assymptotic behaviour for high shear rates (purple line).

A general analytic solution for eqs. (4.33) & (4.34) is not known, but for weak flows $\dot{\gamma} \ll 1/B_g \sim 0.3\,/s$ a solution was obtained analytically by Pedley et al. [54] in the first order of $\epsilon = B_g \omega$. They calculated the stress tensor incorporating all possible shape, gravitational and flow influences, see appendix E, which is linear in the applied shear flow. This results in shear-independent viscosity for small shear rates, which is in good approximation given by

$$\lim_{\dot{\gamma} \ll 1/B_g} \frac{\eta_{eff}}{\eta_0} = 1 + 2.6\phi + \frac{9B_g U}{4a} \phi f(D_r, B_g) \,, \tag{4.37}$$

41
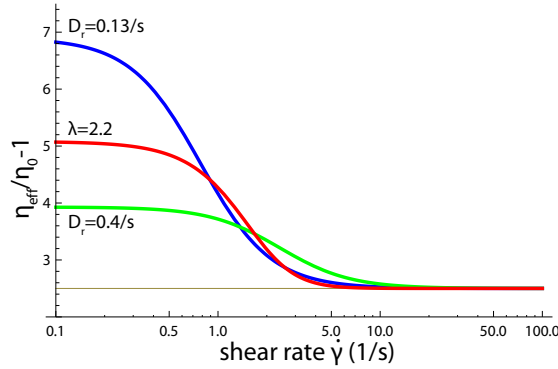
Figure 4.19: Effective viscosity versus volume fraction. Non-gyrotactic swimmers with $D_r = 0.13$ /s (blue) and $D_r = 0.4$ /s (green). Gyrotactic swimmers with $\lambda = 2.2$ (red).

with $f(D_r, B_g) \sim 0.4$, depending on the gravitational orientation time B_g. In consecutive work Bees & Pedley et al. [5] obtained the tensor **Q** by using a spherical harmonics expansion for a single value of $\lambda = 1/(2BD_r) = 2.2$. Substituting their result in (4.27) yields a viscosity which is plotted as the red line in figure 4.19. As a comparison two curves are shown of eq. (4.36), as already plotted in figure 4.18. All three curves are qualitatively similar, but with the zero shear rate viscosity depending on the graviational orientation time B_g, instead of rotary diffusion when taking into account gravity.

Due to the many parameters $(a, b, \epsilon, D_r, B_g, U)$ of the theory as presented here it is hard to draw any quantitative conclusions. Nonetheless qualitatively three regimes can be distinghuised. For high shear rates $\dot{\gamma} > \dot{\gamma}_c$ the swimming speed of the cells becomes negligible to the ambient flow and passive behaviour is expected $\lim_{\dot{\gamma} \gg \dot{\gamma}_c} \frac{\eta_{eff}}{\eta_0} = 1 + \frac{5}{2}\phi$. For small shear rates $1/B_g \gg \dot{\gamma}$ or $D_r \gg \dot{\gamma}$ the viscosity is given by the zero-shear rate viscosity of the form:

$$\lim_{\dot{\gamma} \ll 1/B_g} \frac{\eta_{eff}}{\eta_0} = \lim_{\dot{\gamma} \gg \dot{\gamma}_c} \frac{\eta_{eff}}{\eta_0} + C_B \frac{B_g U}{a} \text{ or}$$

$$\lim_{\dot{\gamma} \ll D_r} \frac{\eta_{eff}}{\eta_0} = \lim_{\dot{\gamma} \gg \dot{\gamma}_c} \frac{\eta_{eff}}{\eta_0} + C_D \frac{U}{a D_r} \,, \tag{4.38}$$

where C_B and C_D dimensionless constants of order unity. For intermediate shear rates $\dot{\gamma}_c > \dot{\gamma} > 1/B_g$ or $\dot{\gamma}_c > \dot{\gamma} > D_r$ an increase of the effective viscosity occurs with decreasing shear rate and

$$\lim_{\dot{\gamma} \gg \dot{\gamma}_c} \eta_{eff} > \eta_{eff} > \lim_{\dot{\gamma} \ll (D_r, 1/B_g)} \eta_{eff} \,. \tag{4.39}$$

A literature study on the statistical description of the orientation of *Chlamydomonas*, whereby it is modeled as prolate spheroid, leads to the conclusion that the swimming motion increases the effective viscosity. The magnitude of the increase depends on the applied shear rate.

4.6 Rheological experiments on *Chlamydomonas*

Rafai et al. [59] measured the effective viscosity for suspensions of *Chlamydomonas* Reinhardtii with a cone-plate rheometer. Shear thinnning occurs for active suspensions, see figure 4.20a . For small shear rates $\dot{\gamma} < 10$ /s a clear increase is observed which qualitatively agrees with theory. The linear theory underestimates the high shear behaviour, but the volume fractions are in the
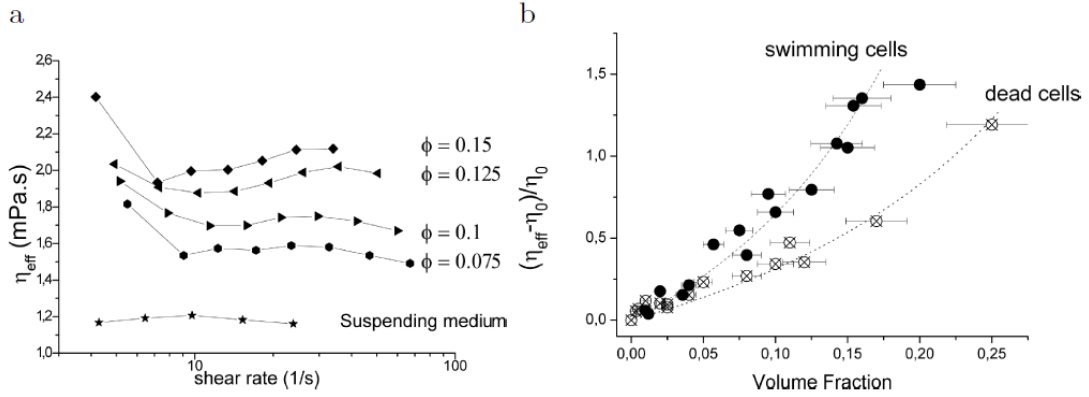
Figure 4.20: a) The effective viscosity as a function of the shear rate for 4 different volume fractions of living *Chlamydomonas* and the suspending medium. b) The effective viscosity of a suspension of active (living) and inactive (dead) *Chlamydomonas*, as a function of volume fraction. Taken from [59].

Table 4.1

Linear effective viscosity constant B for $\dot{\gamma} = 5$ /s	
rigid spheres	2.5
ellipsoid r=1.3	2.4-2.6
ellispoid r=1.7	2.2-2.8
gyrotactic spheres	2.6
Haines	2.8
Pedley	2.9

semi-dilute regime in which the theory is not expected to be valid anymore. Both suspensions of active and inactive particles show an increase of the viscosity with respect to the viscosity of the suspending medium η_0 for a shear rate $\dot{\gamma} = 5$ /s see figure 4.20b . Theoretical predictions for the linear coefficient at this shear rate are listed in table 4.1.

Only small deviations of the spherical value are to be expected. Due to the high scattering and very few data points for active and passive suspensions for low volume fractions $\phi < 5\%$, no conclusion can be drawn about the difference between active and passive suspensions. The theory as presented in the last section can thus not be tested.

For higher volume fractions the difference between active and passive suspensions is clear, both displaying a nonlinear increase. The active suspension shows the biggest increase. The results were fitted using the Krieger-Dougherty relation [40]

$$\frac{\eta_{eff}}{\eta_0} = \left(1 - \frac{\phi}{\phi_{max}}\right)^{-\phi_{max}B} , \qquad (4.40)$$

where ϕ_{max} the maximum packing fraction set to the maximum random packing fraction 0.62 [59]. B is used as a fitting parameter giving $B = 2.5 \pm 0.1$ and $B = 4.5 \pm 0.2$ for inactive and active suspensions respectively. Linear theory underestimates the experimental results for non-dilute volume fractions. The big difference for higher volume fractions indicates that higher order
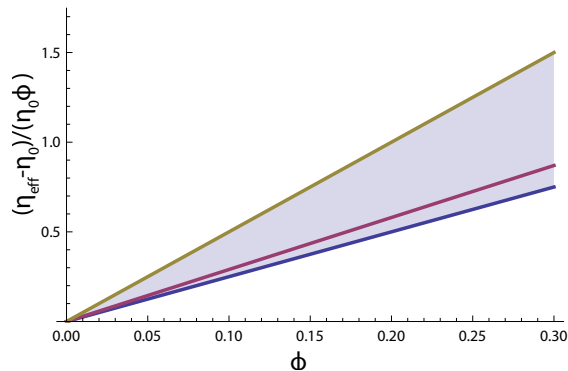
Figure 4.21: The effective viscosity as function of the volume fraction, for passive spheres (blue), the prediction for the active spheres (purple) and the maximum possible viscosity for the active suspensions (yellow).

terms $\sim \phi^n, n > 1$ play a significant role. This non-linearity will be discussed in the last two sections of this chapter. The maximum volume fraction of active suspensions in the experiments is 20%. Which is smaller than the onset of collective behaviour which is $\phi \sim 30\%$ [35] for *Chlamydomonas*. For small aspect ratio particles like *Chlamydomonas* nematic ordering does not occur for low volume fractions $< 30\%$. Hence liquid crystal theory and collective behaviour will not be discussed here.

4.7 Numerical modelling of swimmer suspensions

Ishikawa and Pedley [33] modeled a semi-dilute suspension of squirmers (see appendix F). The experimental set-up of Rafai et al. with $\dot{\gamma} = 5/s$ corresponds to their dimensionless gravity, swimming speed and stresslet strength being $G_{bh} = 2.5$, $Sq = 1.5$ and $\beta = 3$. Without gravity the suspension of swimming spheres with a volume fraction $\phi = 10\%$ is undistinguishable from that of a suspension of passive spheres. Gravity has little effect at high shear rates $G_{bh} < 10$, like for the passive spheres of section 4.3.2. However, for low shear rates $G_{bh} \geq 10$ the viscosity starts to deviate from that of passive particles. Figure 27 shows in [33] shows that for $G_{bh} = 3$ the squirming (=stresslet) stress is negligible. A suspension of the spherical microswimmers in absence of gravitational effects is undistinghuisable from that of passive spheres, regardless of swimming speed. No preferred swimming direction is observed.

4.8 Rheology of non-dilute suspensions of *Chlamydomonas*

Theories of the form

$$\frac{\eta_{eff}}{\eta_0} = 1 + 2.5\phi + \kappa\phi^2 \,, \tag{4.41}$$

incorporating particle interactions, (rotary) diffusion etc. are ubiqitious. They result in a range of second-order coefficients $\kappa = 2.5 - 14.1$, for an overview see [16, 49]. Experimental data show a range of second-order terms too: $\kappa = 4 \pm 2$ [17].

In this chapter two new derivations for the effective viscosity were presented, which both agree with literature. Furthermore a review was provided of the available theoretical work for the effective viscosity of suspensions of both swimming and non-swimming *Chlamydomonas*

cells. The only available experimental results were conducted at a high shear rate at which the difference in effective viscosity of active and inactive suspensions is negligible.

Chapter 5

Conclusion & discussion

Microscopic behaviour of a single cell: Based on an analysis of the cell architecture a new hypothesis for the flagellar synchronisation was formulated. The two flagella are connected both via the basal body and the distal striated fiber. It is not unlikely that this coupling has a bigger effect on synchronisation than hydrodynamic interactions. This might be investigated by modelling the flagella as two driven oscillators connected by a Hookean spring. Also, the coupling through the mutual connection to the cell body, which can rotate and translate, could be responsible for the observed synchronisation. Again, this might be modeled by using two driven oscillators which are connected to a spherical cell body which can rotate and translate, a starting point could be the analysis of the coupled clocks of Huygens [6].

On the microscopic scale of a single Chlamydomonas cell the analytic three-point-force model was extended with a qualitative analysis of the flagellar stroke to incorporate the movement of the flagella. A simple effective and recovery stroke was derived, where the forces are exerted parallel to the swimming direction. The flow field is a superposition of three stokeslets. A comparision was made with the experiments of Guasto et al. [23] on *Chlamydomonas* swimming in a thin film. The latter is best described as a 2D fluid, therefore the 2D stokeslet was used. The full details of the flow field are reproduced during both the effective and recovery stroke.

Macroscopic rheology: On a macroscopic scale the effective viscosity of a dilute suspension of Chlamydomonas has been addressed. For immotile cells the almost spherical cell body leads to a viscosity like for a suspension of passive rigid spheres. At low shear rates $(> 1/s)$ the gravitational couple increases the viscosity. Two new derivations have been presented for the effective viscosity of a dilute suspension of swimming Chlamydomonas cells. One along the theory of Einstein, the other based on the volume average approach of Landau & Lifshitz. Both results are in agreement with literature. The effective viscosity depends on the average orientation of the cells. Based on a literature study, three regimes can be determined. For low shear rates the viscosity is described by the zero shear rate viscosity which is higher than for a suspension of passive particles due to the puller type swimming and the elongated body shape. For intermediate shear rates the viscosity decreases with shear rate. For high shear rates an active suspension behaves like a passive suspension of rigid spheres. This theory is valid for dilute suspensions $\phi < 2\%$ where particle interactions are negligible. The high number of parameters of the theory

requires simultaneous analysis of the following cell properties:

- Size and aspect ratio of the particles;

- Swimming speed;

- Dipole length;

- Rotational diffusion;

- Centre of mass offset.

Many of these parameters not only differ among different strains, but also among cells of the same population. The swimming speed, dipole length and rotational diffusion depend on the environmental conditions too.

The single experiment on the viscosity of suspensions of swimming *Chlamydomonas* of Rafai et al. [59] was conducted at high shear rate where the difference between swimming and non-swimming suspensions is small. Due to the very few scattered data points in the dilute limit, no conclusion can be drawn on the validity of the theory at this shear rate. Experiments at low shear rates should reveal a larger difference. Theories incorporating higher order contributions (ϕ^n) for simple passive systems do exist but show a wide variety of results. It is not to be expected that for the more complex active systems theories for volume fractions of more than 2% will have any validity.

The interference of the flagellar movement and the applied shear flow not yet clear. It might affect the swimming orientation of the cells. The underlying problem is that, although the flagellar movement is well recorded, the internal 'algorithm' or switching mechanism responsible for the beating pattern remains a mystery. This is an interesting field of research in itself.

Appendix A

Acknowledgment

Appendix B

Technology assessment

With the current focus on algae as a basis for feed, coatings, hydrogen producer, etc. it is evident that a deeper understanding of both microscopic and macroscopic properties of suspensions of *Chlamydomonas* is necessary. An application of the rheological theory would be for motility measurements. First the number density of swimmers has to be obtained. *Chlamydomonas* has a slight density excess over water, by measuring the mass density of the suspension the mass fraction of *Chlamydomonas* is obtained. The mass of a single cell is known, thus the number density can be calculated. The motility can then be measured by measuring the viscosity, for example with a rheometer. The viscosity-motility relation can for dilute suspension be determined analytically, but for higher suspensions a semi-empirical approach will be more usefull. This technique is not limited to *Chlamydomonas*, but could also be used in hospitals to determine the motility quality of human spermatozoa.

Appendix C

Hydrodynamics

Incompressible fluid dynamics is described by the Navier-Stokes equation

$$\rho \left(\frac{\partial \vec{u}}{\partial t} + \vec{u} \cdot \nabla \vec{u} \right) = -\nabla p + \eta \nabla^2 \vec{u} + \vec{F} \,, \tag{C.1}$$

with $\vec{F}$ the external body forces and ρ and η the density and viscosity of the fluid respectively. Let us consider a submerged object of size L translating with speed U. The Navier-Stokes equation eq. (C.1) can then be nondimensionalised by using the object speed and size, the viscosity and the density of the fluid. With

$$
\begin{aligned}
\vec{u} &= U\vec{u}' \\
\frac{\partial}{\partial t} &= \frac{U}{L}\frac{\partial}{\partial t'} \\
\nabla &= \frac{\nabla'}{L} \\
p &= \frac{\eta U L}{L^2} p' \\
\vec{F} &= \frac{\eta U L}{L^3} \vec{F}'
\end{aligned}
\tag{C.2}
$$

eq. (C.1) can be recast as

$$\frac{\rho U L}{\eta} \left(\frac{\partial \vec{u}'}{\partial t'} + \vec{u}' \cdot \nabla' \vec{u}' \right) = -\nabla' p' + (\nabla')^2 \vec{u}' + \vec{F}' \,. \tag{C.3}$$

The prefactor $\frac{\rho U L}{\eta}$ is the Reynolds number (Re). For $Re \ll 1$ the Navier-Stokes equation reduces to the Stokes equation

$$-\nabla p + \eta \nabla^2 \vec{u} = \vec{F} \,. \tag{C.4}$$

This is a time indepedent equation, the fluid flow at any moment in time is uniquely defined by the boundary conditions. A force monopole at the origin is mathematically described as

$$-\nabla p + \eta \nabla^2 \vec{u} = \vec{F}\delta(r) \,, \tag{C.5}$$

which can be solved by using e.g. Greens function theory to give the Stokeslet solution

$$\vec{u}_{Sto}(\vec{r}) = \mathbf{T}(\vec{r}) \cdot \vec{F} \,, \ \mathbf{T}(\vec{r}) = \frac{1}{8\pi\eta r} \left(\mathbf{I} + \frac{\vec{r} \otimes \vec{r}}{r^2} \right) \,, \tag{C.6}$$

with $\mathbf{I}$ the unit tensor and $\otimes$ the tensorial or Kronecker product. A force dipole of strength S is a superposition of two point forces $\vec{F}$ and $-\vec{F}$ a length b apart and induces a stresslet

$$\vec{u}_s = -\frac{3}{8\pi\eta} \frac{\mathbf{S} : (\hat{r} \otimes \hat{r})}{r^2} \hat{r} \,, \tag{C.7}$$

with $\hat{p}$ the unit vector along the line joining the points at which the two point forces are exerted. The stresslet tensor is

$$\mathbf{S} = S\,(\hat{p} \otimes \hat{p} - \mathbf{I}/3)\,. \tag{C.8}$$

Eq. (C.7) can be derived by taking the limit of two stokeslets of strength F for vanishing distance d between the acting point forces but remaining a constant $S = Fd$. Eq. (C.7) can be recasted as

$$\vec{u}_s = -\frac{S}{8\pi\eta}\frac{1 - 3(\hat{p}\cdot\hat{r})^2}{r^2}\hat{r}\,, \tag{C.9}$$

with $1 - 3(\hat{p}\cdot\hat{r})^2 = 1 - 3\cos^2\theta = P_2(\cos\theta)$, where $P_2(x)$ is the second Legendre polynom. In the same manner a quadrupole with direction along the unit vector $\hat{p}$ at the origin with strength Q induces (in leading order) a source doublet field

$$\vec{u}_{SD}(\vec{r}) = \frac{Q}{4\pi\eta r^3}\left(\mathbf{I}/3 - \frac{\vec{r}\otimes\vec{r}}{r^2}\right)\cdot\hat{p}\,. \tag{C.10}$$

The aforementioned flow fields are obtained for an unbound fluid volume in 3D. Certain thin films show (quasi-)2D behaviour. Solving eq. (C.4) for a point force in 2D yields the 2D stokeslet

$$\vec{u}_{Sto2D}(\vec{r}) = \mathbf{T}(\vec{r})\cdot\vec{F}\,,\ \mathbf{T}(\vec{r}) = \frac{1}{4\pi\eta}\left(-ln(r/r_0)\mathbf{I} + \frac{\vec{r}\otimes\vec{r}}{r^2}\right)\,. \tag{C.11}$$

where r_0 is an arbitrary length scale. Let us consider two point forces exerted in opposite direction. The first at the origin, the second at a point $\vec{r}_1$. The flow field is then described as

$$\vec{u}_{Sto2D}(\vec{r}) = \frac{F}{4\pi\eta}\left([-ln(r/r_0) + ln(|r - \vec{r}_1|/r_0)]\mathbf{I} + \frac{\vec{r}\otimes\vec{r}}{r^2} - \frac{(\vec{r}-\vec{r}_1)\otimes(\vec{r}-\vec{r}_1)}{r^2}\right)\,. \tag{C.12}$$

and can be rewritten as

$$\vec{u}_{Sto2D}(\vec{r}) = \frac{F}{4\pi\eta}\left(ln(|r - \vec{r}_1|/r)\mathbf{I} + \frac{\vec{r}\otimes\vec{r}}{r^2} - \frac{(\vec{r}-\vec{r}_1)\otimes(\vec{r}-\vec{r}_1)}{r^2}\right)\,. \tag{C.13}$$

A derivation of these flow fields is given in the book of Pozrikidis [56]. Along the same lines the two dimensional stresslet can be derived

$$\vec{u}_{Str2D} = \frac{1}{4\pi\eta r}(1 - 2(\hat{p}\cdot\hat{r})^2)\hat{r}\,. \tag{C.14}$$

This result can be obtained by a multipole expansion of two stokeslets using

$$ln(\frac{r}{r - r_1}) = 0 - \frac{\vec{r}_1\cdot\vec{r}}{r^2}\,. \tag{C.15}$$

The stresses exerted on a submerged particle can be integrated over the particle surface to give the total force, dipole strength and quadrupole strength

$$\vec{F} = \int \boldsymbol{\sigma}\cdot\hat{n}dA\,, \tag{C.16}$$

$$p'\mathbf{I} + \mathbf{S} + \mathbf{R} = \int \vec{r}\otimes(\boldsymbol{\sigma}\cdot\hat{n})dA\,, \tag{C.17}$$

$$\mathbf{Q} = \int \vec{r}\otimes(\vec{r}\otimes(\boldsymbol{\sigma}\cdot\hat{n}))dA\,. \tag{C.18}$$

The dipole strength is decomposed in an isotropic $p'\mathbf{I}$, a symmetric stresslet $\mathbf{S}$ and an antisymmetric rotlet or couplet $\mathbf{R}$ term

$$p'\mathbf{I} = \int \frac{1}{3}\vec{r} \cdot \boldsymbol{\sigma} \cdot \hat{n} \mathbf{I} dA\,, \tag{C.19}$$

$$\mathbf{S} = \int \left[\frac{1}{2}(\vec{r} \otimes (\boldsymbol{\sigma} \cdot \hat{n}) + (\boldsymbol{\sigma} \cdot \hat{n}) \otimes \vec{r})) - \frac{1}{3}\vec{r} \cdot \boldsymbol{\sigma} \cdot \hat{n} \mathbf{I} - \eta(\vec{u} \otimes \hat{n} + \hat{n} \otimes \vec{u}) \right] dA\,, \tag{C.20}$$

$$\mathbf{R} = \int \frac{1}{2}(\vec{r} \otimes (\boldsymbol{\sigma} \cdot \hat{n}) - (\boldsymbol{\sigma} \cdot \hat{n}) \otimes \vec{r}) dA\,. \tag{C.21}$$

This decomposition was introduced by Batchelor [3]. The last term in the stresslet is zero for a rigid particle, but by adding this term the integral can be taken over any fluid volume containing one particle. The rotlet can be restated as

$$\mathbf{R} = \frac{1}{2}\epsilon : \tau\,, \tag{C.22}$$

with τ the torque on the particle and ϵ the Levi-Civita permutation tensor. Batchelor [3] showed that the contribution to the stress by the presence of the particle is as follows

$$\boldsymbol{\sigma}_p = \frac{\mathbf{S} + \mathbf{R}}{V}\,. \tag{C.23}$$

Appendix D

Three-point-force model

The velocity field due to a distribution of point forces is a superposition of stokeslets

$$\vec{u}(\vec{r}) = \sum_i \mathbf{T}(\vec{r} - \vec{r}_i) \cdot \vec{F}_i \,, \tag{D.1}$$

where $\vec{F}_i$ being a point force at position r_i and

$$\mathbf{T}(\vec{r}) = \frac{1}{8\pi\eta r} \left(\mathbf{I} + \frac{r \otimes r}{r^2} \right) \,, \tag{D.2}$$

the Oseen tensor. *Chlamydomonas* with its two flagella is modeled as a superposition of three point forces, one at its body centre which we define as the origin. $(0,0,F)$ at $\vec{r}_0 = (0,0,0)$ and two point forces in the xz plane: $(0,0,-F/2)$ at $\vec{r}_{1,2} = (\pm a, 0, b/2)$. The flow due to the superposition of these forces is given

$$\vec{u}(\vec{r}) = \vec{F} \cdot \mathbf{T}_{sum}(\vec{r}) \,, \tag{D.3}$$

with

$$8\pi\eta \cdot \mathbf{T}_{sum}(\vec{r}) = \frac{1}{r} \left(\mathbf{I} + \frac{\vec{r} \otimes \vec{r}}{r^2} \right) - \frac{1}{2} \frac{1}{|\vec{r} - \vec{r}_1|} \left(\mathbf{I} + \frac{(\vec{r} - \vec{r}_1) \otimes (\vec{r} - \vec{r}_1)}{|\vec{r} - \vec{r}_1|^2} \right) \tag{D.4}$$

$$- \frac{1}{2} \frac{1}{|\vec{r} - \vec{r}_2|} \left(\mathbf{I} + \frac{(\vec{r} - \vec{r}_2) \otimes (\vec{r} - \vec{r}_2)}{|\vec{r} - \vec{r}_2|^2} \right) \,. \tag{D.5}$$

The multipole expansion for $r_1 \ll r$

$$\frac{1}{|\vec{r} - \vec{r}_1|} = \frac{1}{r} + \frac{\vec{r}_1 \cdot \vec{r}}{r^3} + O(r^{-5}) \,, \tag{D.6}$$

is used to deduce the $\mathbf{I}$ part of eq. (D.5)

$$\mathbf{I} \left(\frac{1}{r} - \frac{1}{2} \frac{1}{|\vec{r} - \vec{r}_1|} - \frac{1}{2} \frac{1}{|\vec{r} - \vec{r}_2|} \right) = -\frac{1}{2} \frac{(\vec{r}_1 + \vec{r}_2) \cdot \vec{r}}{r^3} \mathbf{I} \tag{D.7}$$

Again by using a multipole expansion

$$\frac{1}{|\vec{r} - \vec{r}_1|^3} = \frac{1}{r^3} + \frac{3\vec{r}_1 \cdot \vec{r}}{r^5} + O(r^{-7}) \tag{D.8}$$
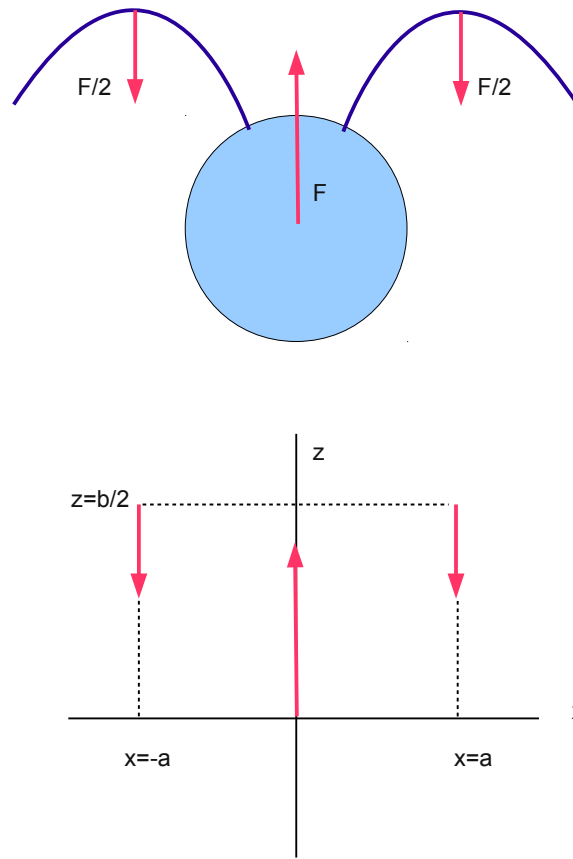
53

Figure D.1: Schematic overview of three-point-force model

the $\vec{r} \otimes \vec{r}$ part of eq. (D.5) is obtained

$$\vec{r} \otimes \vec{r} \left(\frac{1}{r^3} - \frac{1}{2} \left(\frac{1}{|\vec{r} - \vec{r}_1|^3} + \frac{1}{|\vec{r} - \vec{r}_2|^3} \right) \right) = -\frac{3}{2} \frac{(\vec{r}_1 + \vec{r}_2) \cdot \vec{r}}{r^5} \vec{r} \otimes \vec{r}. \tag{D.9}$$

Finally the last part is the cross terms in the dyadic product, whereby $(\vec{r_1} \otimes \vec{r_1})$ can be neglected as it decays like $1/r^3$

$$\sim \left(-\frac{1}{2} \frac{1}{r} \frac{-(r \otimes r_1 + r_1 \otimes r)+}{r^2} - \frac{1}{2} \frac{1}{r} \frac{-(r \otimes r_2 + r_2 \otimes r)+}{r^2} \right)$$

$$\sim \frac{1}{2} \frac{(r \otimes (r_1 + r_2) + (r_1 + r_2) \otimes r)}{r^3} . \tag{D.10}$$

Combining all previous results yields

$$\mathbf{T}_{sum}(\vec{r}) \sim \frac{1}{2} \left(\frac{(\vec{r} \otimes (\vec{r}_1 + \vec{r}_2) + (\vec{r}_1 + \vec{r}_2) \otimes \vec{r})}{r^3} - \frac{(\vec{r}_1 + \vec{r}_2) \cdot \vec{r}}{r^3} (\mathbf{I} + \frac{3\vec{r} \otimes \vec{r}}{r^2}) \right) . \tag{D.11}$$

Note that only the sum of the vectors $\vec{r}_1 + \vec{r}_2$ plays a role, which is restated as a new vector $\vec{r}_3 = \vec{r}_1 + \vec{r}_2 = (0, 0, b)$ so that

$$\mathbf{T}_{sum}(\vec{r}) \sim \frac{1}{2} \left(\frac{\vec{r} \otimes \vec{r}_3 + \vec{r}_3 \otimes \vec{r}}{r^3} - \frac{\vec{r}_3 \cdot \vec{r}}{r^3} \left(\mathbf{I} + \frac{3\vec{r} \otimes \vec{r}}{r^2} \right) \right) . \tag{D.12}$$

The far field for the three-point-force model with force positions $0, \vec{r}_1, \vec{r}_2$ is the same as for two stokeslets at $0, \vec{r}_1 + \vec{r}_2$. This result can be generalised. Let's assume one point force is exerted at the origin, the second one is positioned at $\vec{r}_3 = b\hat{p}$. The forces are then $\vec{F} = \pm F\hat{p}$, where $\hat{p}$ the unit vector along the line joining the point forces.

$$\begin{aligned} \vec{u} &= \frac{bF}{16\pi\eta r^2} \hat{p} \cdot (\hat{r} \otimes \hat{p} + \hat{p} \otimes \hat{r} - \hat{p} \cdot \hat{r} (\mathbf{I} + 3\hat{r} \otimes \hat{r})) \\ &= \frac{bF}{16\pi\eta r^2} (1 - 3(\hat{p} \cdot \hat{r})^2)\hat{r} \end{aligned} \tag{D.13}$$

This is the second spherical harmonic and is known as the stresslet field. In the notation of Batchelor [3] this can be written as

$$\vec{u} = -\frac{3}{8\pi\eta} \frac{\mathbf{S} : (\hat{r} \otimes \hat{r})}{r^2} \hat{r} \tag{D.14}$$

with the stresslet being

$$\mathbf{S} = \frac{bF}{2} \left(\hat{p} \otimes \hat{p} - \mathbf{I}/3 \right) \tag{D.15}$$

Appendix E

Stress tensor

For a Newtonian fluid the stress tensor is

$$\boldsymbol{\sigma} = -p\mathbf{I} + 2\eta\mathbf{e}\,. \tag{E.1}$$

The so called 'Batchelor stresses' due to the presence of an ellipsoidal particle are [3]

$$\boldsymbol{\sigma}_p = 4\eta n v \left[\alpha_1 \mathbf{E} : \langle\hat{p}\hat{p}\hat{p}\hat{p}\rangle + \alpha_2(\mathbf{E}\cdot\langle\hat{p}\hat{p}\rangle + \langle\hat{p}\hat{p}\rangle\cdot\mathbf{E}) + \alpha_3\mathbf{E} + \alpha_4\mathbf{E} : \langle\hat{p}\hat{p}\rangle\mathbf{I}\right]$$
$$+ \frac{n}{2}\left[\epsilon\cdot\langle\vec{L}\rangle + \frac{1}{2}\alpha_0\langle(\hat{p}\times\vec{L})\hat{p} + \hat{p}(\hat{p}\times\vec{L})\rangle\right]\,, \tag{E.2}$$

where $\vec{L} = -\rho v h \hat{p} \times \vec{g}$ is the gravitational torque for a body of volume v, gravity offset h and $\vec{g}$ gravity acceleration. The functions α_i depend the aspect ratio, and ϵ is the alternating tensor. The short hand notation for the Kronecker product is used $\vec{a} \otimes \vec{b} = \vec{a}\vec{b}$ and $\langle..\rangle$ denotes the ensemble average. Rotary diffusion leads to a stress given by

$$\boldsymbol{\sigma}_d = 2\eta n v D_r \alpha_5(\langle\hat{p}\otimes\hat{p}\rangle - \mathbf{I}/3)\,. \tag{E.3}$$

The swimming of an object yields

$$\boldsymbol{\sigma}_s = S(\langle\hat{p}\otimes\hat{p}\rangle - \mathbf{I}/3)\,. \tag{E.4}$$

Combining the previous equations leads to a total stress

$$\boldsymbol{\sigma} = -p + 2\eta\mathbf{e} + \boldsymbol{\sigma}_p + \boldsymbol{\sigma}_s + \boldsymbol{\sigma}_d\,. \tag{E.5}$$

The diffusive and swimming term can be combined [29]

$$\boldsymbol{\sigma}_{sd} = (S + 2\eta n v \alpha_5 D_r)(\langle\hat{p}\otimes\hat{p}\rangle - \mathbf{I}/3)\,. \tag{E.6}$$

The ratio of swimming and diffusion term is

$$\beta = \frac{6\pi\eta a U b}{2\eta v D_r \alpha_5} \sim 10^3\,. \tag{E.7}$$

For passive rotary diffusion $\beta \sim 10^3$ and for active rotary diffusion $\beta \sim 50$. At small shear rates $\epsilon = B\omega \ll 1$ the stress tensor has been derived analytically [54] in the first order of the strain rate as

$$\sigma_{xy,p} + \sigma_{xy,sd} = \frac{\eta_0\phi\dot{\gamma}\alpha_\perp}{8}\left(\frac{9\eta_0 U}{h\rho g a}\frac{b}{a}(J_2 - 2\alpha_0 J_5) + 2.6\right)\,, \tag{E.8}$$

where their constant $\alpha_F = 1$. $\alpha_0 \sim 0.3$ is the aspect ratio minus one and $\alpha_\perp \sim 7$ a constant which depends on aspect ratio. $J_i = J_i(\lambda)$ are functions of the parameter $\lambda = (2BD_r)^{-1}$.

The linear viscosity coefficient is then

$$B = \left(\frac{\eta_{eff}}{\eta_0} - 1 \right) / \phi = \frac{9\eta_0 \alpha_\perp U}{8h\rho g a} \frac{b}{a} (J_2 - 2\alpha_0 J_5) + 2.6 \,. \tag{E.9}$$

The latter term $(J_2 - 2\alpha_0 J_5) \sim 0.4$ for $\lambda = 2.2$ [54].

Appendix F

Squirmer: a theoretical swimmer
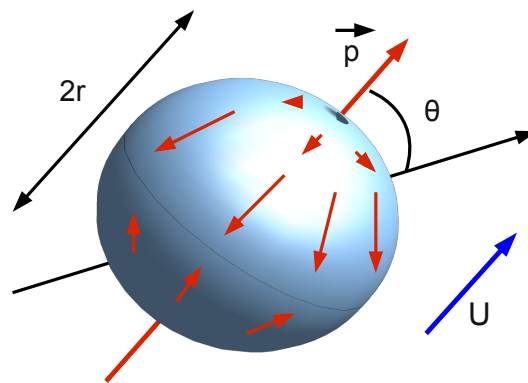
Figure F.1: A puller type squirmer with radius r, director p and swimming with a speed U.

In 1952 Lighthill [44] introduced an axisymmetric rigid spherical swimmer by applying the following boundary conditions on the surface of a sphere

$$u_r = \sum_{n=1}^{\infty} A_n P_n(\cos\theta), \qquad (F.1)$$

u_r being the radial velocity, and the azimuthal velocity component

$$u_\theta = B_1 \sin\theta + \frac{B_2}{2} \sin(2\theta) + \sum_{n=3}^{\infty} B_n sin(n\theta), \qquad (F.2)$$

where θ is the azimuthal angle with the director of the squirmer. Blake [8] extended the work of Lighthill. The B_1-term determines the swimming speed $U = \frac{2}{3}B_1$, the B_2 term determines the type of swimmer (pusher/puller). Without loss of generality we can state $B_1 > 0$. For a puller $B_2 > 0$ and for a pusher $B_2 < 0$. The higher order terms and the radial boundary conditions do

not change this general behaviour and are thus neglected ($A_m = B_n = 0$ for $n > 2$ and $m > 0$). For a single squirmer in a non-moving Newtonian fluid the velocity is obtained by solving the Stokes equation

$$u_r = -\frac{2}{3}B_1 \cos(\theta) + \frac{2}{3}B_1 \left(\frac{a}{r}\right)^3 P_1(\cos(\theta)) + \left(\left(\frac{a}{r}\right)^4 - \left(\frac{a}{r}\right)^2\right) B_2 P_2(\cos(\theta)), \quad \text{(F.3)}$$

where $P_n(x)$ denotes the n-th Legendre polynomial i.e. $P_1(x) = x$, $P_2(x) = \frac{1}{2}(3x^2 - 1)$. The azimuthal velocity component is

$$u_\theta = \frac{2}{3}B_1 \sin(\theta) + \frac{B_1}{3}\left(\frac{a}{r}\right)^3 V_1(\cos(\theta)) + \frac{1}{2}\left(\frac{a}{r}\right)^4 B_2 V_2(\cos(\theta)), \quad \text{(F.4)}$$

where $V_1(\cos(\theta)) = \sin(\theta)$ and $V_2(\cos(\theta)) = \sin(\theta)\cos(\theta)$. Setting $r = a$ one easily sees that this obeys the boundary conditions. The swimming speed is related to the first coefficient $U = \frac{2}{3}B_1$. The induced flow field can also be restated as:

$$\vec{u}_s = B_1 \left(\frac{a}{r}\right)^3 \left(\frac{\hat{p}\cdot\vec{r}}{r}\hat{r} - \frac{\hat{p}}{3}\right) + \left(\left(\frac{a}{r}\right)^4 - \left(\frac{a}{r}\right)^2\right) B_2 P_2 \left(\frac{\hat{p}\cdot\vec{r}}{r}\right)\hat{r} + \left(\frac{a}{r}\right)^4 B_2 \frac{\hat{p}\cdot\vec{r}}{r}\left(\frac{\hat{p}\cdot\vec{r}}{r} - \hat{p}\right)$$
$$\text{(F.5)}$$

The far field (up to $1/r^2$) for a squirmer is a stresslet, the radial velocity component is

$$u_r = -\frac{2}{3}B_1 \cos(\theta) - \left(\frac{a}{r}\right)^2 B_2 P_2(\cos(\theta)). \quad \text{(F.6)}$$

and the azimuthal component is

$$u_\theta = \frac{2}{3}B_1 \sin(\theta). \quad \text{(F.7)}$$

Appendix G

Einstein derivation of the effective viscosity of a suspension of *Chlamydomonas*

For dilute suspensions particle interactions are negligible, the many particle problem thereby reduces to a single particle problem. Any arbitrary flow can be decomposed in a rotational, dilatational and linear component. A spherical particle instanteneously rotate and translate with the ambient fluid, but will affect the dilatational part of the flow. The latter is denoted as

$$\vec{u}_0 = \mathbf{e}_0 \cdot \vec{r}, \tag{G.1}$$

with the strain rate tensor

$$\mathbf{e}_0 = \begin{bmatrix} A & 0 & 0 \\ 0 & B & 0 \\ 0 & 0 & C \end{bmatrix}. \tag{G.2}$$

Incompressibility of the flow $(\nabla \cdot \vec{u})$ requires $Trace(\mathbf{e}_0) = 0$. The particle reflects the flow via the no-slip boundary conditions, leading to a distortion field:

$$\vec{u}_1 = -\frac{5}{2} \left(\frac{a^3}{r^3} - \frac{a^5}{r^5} \right) \frac{\vec{r} \cdot (\mathbf{e}_0 \cdot \vec{r})}{r^2} \vec{r} + \frac{a^5}{r^5} \mathbf{e}_0 \cdot \vec{r}. \tag{G.3}$$

The total field outside the particle is then:

$$\vec{u} = \vec{u}_0 + \vec{u}_1. \tag{G.4}$$

The work done on a large fluid volume containing the particle is compared with the same fluid volume containing a homogeneous liquid. The work on a sphere in a fluid volume V can be calculated by taking the following surface integral over the boundary of the fluid volume:

$$W = \int (\boldsymbol{\sigma} \cdot \hat{n}) \cdot \vec{u} dS, \tag{G.5}$$

where S is the surface boundary of the volume V and $\hat{n}$ the surface normal and $(\boldsymbol{\sigma} \cdot \hat{n})$ is the force exerted on the surface. The volume V is chosen to be a cocentric infinitely large sphere. With

$\sigma \sim U/r$, $\int dS \sim r^2$ and $u_0 \sim r$, in this case only the terms in $u_1 \sim 1/r^2$ give a contribution in the first order of the volume fraction. To obtain the result for many suspended particles the integral is evaluated and multiplied with the number density of suspended particles

$$\frac{W}{V} = 2\eta_0 \left(1 + \frac{1}{2}\phi\right) \mathbf{e}_0 : \mathbf{e}_0 \,, \tag{G.6}$$

with ϕ the volume fraction of suspended particles. The double dot product of two tensors is defined as $\mathbf{a} : \mathbf{b} = \sum_{i,j} a_i b_i$. Due to the presence of the particles the volume average strain tensor is modified too. Taking the volume average over the same volume V gives

$$\mathbf{e} = \frac{1}{V} \int \frac{1}{2} (\nabla + \nabla^T) \vec{u} dV = \mathbf{e}_0 + \frac{1}{V} \int \nabla \vec{u}_1 dV = (1 - \phi)\mathbf{e}_0 \,. \tag{G.7}$$

Substituting in eq. (G.6) yields

$$\frac{W}{V} = 2\eta_0 \frac{1 + \frac{1}{2}\phi}{(1 - \phi)^2} \mathbf{e} : \mathbf{e} \,. \tag{G.8}$$

If the volume would contain a homogeneous fluid the work on the sphere would be described by

$$\frac{W}{V} = 2\eta_{eff} \mathbf{e} : \mathbf{e} \,. \tag{G.9}$$

Introducing the effective viscosity η_{eff} allows us to treat the suspension as a homogeneous fluid

$$\frac{\eta_{eff}}{\eta_0} = \frac{1 + \frac{1}{2}\phi}{(1 - \phi)^2} \simeq 1 + \frac{5}{2}\phi \,, \tag{G.10}$$

For a microswimmer the effective viscosity will be derived along the same lines as for the passive sphere. The far field of any swimming force-free organism or object is a stresslet field, of strength

$$D = \frac{bF}{16\pi\eta} \,. \tag{G.11}$$

$$\vec{u}_s = -\frac{D}{r^2}(1 - 3\cos^2\theta)\hat{r} \,. \tag{G.12}$$

The total flow field is a superposition of the applied shear flow, the disturbance flow due to the presence of the particle and the swimmer stresslet flow

$$\vec{u} = \vec{u}_{shear} + \vec{u}_{sph} + \vec{u}_s(\hat{p}) \,, \tag{G.13}$$

The mechanical work on a large fluid volume containing the particle is

$$W = c \int_{r \to \infty} (\boldsymbol{\sigma} \cdot \hat{n}) \cdot \vec{u} dS \,. \tag{G.14}$$

And the correction in the strain rate is given as

$$\mathbf{E}^* = \mathbf{E} - c \int \nabla \cdot \vec{u} dU = \mathbf{E} - c \int_{r \to \infty} \frac{\vec{u}}{r} \cdot \hat{n} dS \,. \tag{G.15}$$

A dilatational flow field with the axis of the cartesian coordinate system coinciding with the 3 dilatational directions is described by $\vec{u}_{shear} = \mathbf{E} \cdot \vec{r}$, with

$$\mathbf{E} = \begin{pmatrix} A & 0 & 0 \\ 0 & B & 0 \\ 0 & 0 & C \end{pmatrix} \,. \tag{G.16}$$

61

In leading order the stress tensor of stresslet has two non-zero terms in spherical coordinates

$$\boldsymbol{\sigma}_s = \begin{pmatrix} \sigma_{s,rr} & \sigma_{s,r\theta} & 0 \\ 0 & 0 & 0 \\ 0 & 0 & 0 \end{pmatrix},$$

(G.17)

whereby $\sigma_{s,rr} = \eta D \frac{2(1-3\cos^2\theta)}{r^3}$ and $\sigma_{s,r\theta} = \eta D \frac{(-3\sin\theta\cos\theta)}{2r^3}$. The terms in eq. (G.14) involving only passive contributions were calculated in section 4.4. The only two terms involving the swimmer flow that give a contriubtion in the first order of ϕ are

$$W_1 = \frac{n}{U} \int (\sigma_{s,rr} u_{shear,r} + \sigma_{s,\theta} u_{shear,\theta}) dS\,,$$

(G.18)

leading to

$$\frac{W_1}{\eta U} = \frac{3}{5} \frac{D\phi}{a} \left(\vec{p} \otimes \vec{p} - \frac{\mathbf{I}}{3} \right) : \mathbf{E}\,.$$

(G.19)

Combining with the Einstein result of eq. (G.6) yields the total work on the sphere

$$\frac{W_{total}}{\eta U} = \left(1 + \frac{\phi}{2} \right) \mathbf{E} : \mathbf{E} + \frac{3}{5} \frac{D\phi}{a} \left(\vec{p} \otimes \vec{p} - \frac{\mathbf{I}}{3} \right) : \mathbf{E}\,.$$

(G.20)

The second integral eq. (G.15) involving the correction of the strain rate is given by

$$\mathbf{E}^* = \mathbf{E}(1-\phi) - \mathbf{R} \cdot \frac{\phi D}{a} \boldsymbol{\beta} \cdot \mathbf{R}^T = \mathbf{E}(1-\phi) + \frac{6}{5} \frac{D\phi}{a} \left(\vec{p} \otimes \vec{p} - \frac{\mathbf{I}}{3} \right)\,.$$

(G.21)

The double dot product of the strain can then be recasted as

$$\mathbf{E} : \mathbf{E} = \frac{\mathbf{E}^* : \mathbf{E}^*}{(1-\phi)^2} + \frac{12}{5} \frac{\phi D}{a(1-\phi)^2} \left(\vec{p} \otimes \vec{p} - \frac{\mathbf{I}}{3} \right) \mathbf{E}^* + O(\phi^2)\,.$$

(G.22)

Substituting this result in eq. (G.20) yields the total work on the sphere as a function of the actual strain rate

$$\begin{aligned} \frac{W_{total}}{\eta V} =& \left(1 + \frac{\phi}{2} \right) \left(\frac{\mathbf{E}^* : \mathbf{E}^*}{(1-\phi)^2} + \frac{12}{5} \frac{\phi D}{a(1-\phi)^2} \left(\vec{p} \otimes \vec{p} - \frac{\mathbf{I}}{3} \right) \right) \mathbf{E}^* \\ &+ \frac{3}{5} \frac{D\phi}{a(1-\phi)} \left(\vec{p} \otimes \vec{p} - \frac{\mathbf{I}}{3} \right) : \left(\mathbf{E}^* + \frac{6}{5} \frac{D\phi}{a} \left(\vec{p} \otimes \vec{p} - \frac{\mathbf{I}}{3} \right) \right)\,. \end{aligned}$$

(G.23)

This can be expanded in first order of ϕ to give

$$\frac{W_{total}}{\eta V} = \left(1 + \frac{5}{2}\phi \right) \mathbf{E}^* : \mathbf{E}^* + 3 \frac{\phi D}{a} \left(\vec{p} \otimes \vec{p} - \frac{\mathbf{I}}{3} \right) : \mathbf{E}^*\,.$$

(G.24)

The work on the sphere depends on the swimming orientation with respect to the applied shear flow. In e.g. a cone-plate rheometer the shear viscosity is measured. For a simple shear flow the strain rate tensor is:

$$\mathbf{E}^* = \begin{pmatrix} 0 & \dot{\gamma} & 0 \\ 0 & 0 & 0 \\ 0 & 0 & 0 \end{pmatrix}\,.$$

(G.25)

The measured viscosity is deduced from eq. (G.24)

$$\frac{\eta_{eff}}{\eta_0} = \left(1 + \frac{5}{2}\phi \right) + 3 \frac{\phi D}{\dot{\gamma} a} p_x p_y\,.$$

(G.26)

Combining with eq. (G.12) yields the effective viscosity in first order of the volume fraction for a spherical microswimmer

$$\frac{\eta_{eff}}{\eta_0} = 1 + \left(\frac{5}{2} + \frac{9}{4} \frac{b}{a} \frac{U}{a\dot{\gamma}} p_x p_y \right) \phi\,.$$

(G.27)

Appendix H

Volume average effective viscosity of a suspension of *Chlamydomonas*

The volume average method of Landau & Lifshitz [41] is briefly presented here, first for passive spheres, later on for microswimmers. In the dilute limit the many particle problem reduces to a single particle suspended in an unbound dilatational flow $\vec{u} = \mathbf{E} \cdot \vec{r}$. The stress tensor is averaged over a big sphere V containing the small particle

$$\langle \boldsymbol{\sigma} \rangle = \frac{1}{V} \int \boldsymbol{\sigma} \, dV \,, \tag{H.1}$$

This expression can be restated as

$$\langle \boldsymbol{\sigma} \rangle = -\langle p \rangle \mathbf{I} + \eta_0 \underbrace{(\nabla \langle \vec{u} \rangle + (\nabla \langle \vec{u} \rangle)^T)}_{2\langle \mathbf{E} \rangle} + \int_V \left(\boldsymbol{\sigma} - \eta_0 (\nabla \vec{u} + (\nabla \vec{u})^T) + p\mathbf{I} \right) dV \,. \tag{H.2}$$

The first terms two terms denote the Newtonian behaviour of the fluid outside the particle, the latter integral is a measure of the internal stress within the rigid sphere. It is strictly zero within the fluid. The analysis of the internal stresses within the particle is possible, but it is simpler to convert the volume integral into a surface integral by using the identitie

$$\boldsymbol{\sigma} = \nabla \cdot (\boldsymbol{\sigma} \otimes \vec{r}) \,, \tag{H.3}$$

and the theorem of Gauss

$$\int (\nabla \cdot \mathbf{F}) dV = \int \mathbf{F} \cdot n \, dS \,, \tag{H.4}$$

$$\int (\nabla \mathbf{F}) dV = \int \mathbf{F} \otimes \hat{n} \, dS \,. \tag{H.5}$$

The volume integral in eq. (H.2) is then recast as

$$\int_S \left((\boldsymbol{\sigma} \otimes \vec{r}) \cdot \hat{n} - \eta (\vec{u} \otimes \hat{n} + \hat{n} \otimes \vec{u}) \right) dS \,, \tag{H.6}$$

where is S the surface boundary of the volume V. The pressure term in the integral drops out. Note that this equation is linear in the velocity $\vec{u}$ and is the same as the stresslet of Batchelor (C.20) except for the uninteresting isotropic part. Thus this integral can be calculated over both the surface of the particle, but it is often easier to choose a large volume containing a small particle. The solution of the integral for tiny rigid spheres is given in [41], using this result to calculate the part in eq. (H.2) involving the strain rate yields

$$\langle \boldsymbol{\sigma} \rangle = \eta_0 \langle \mathbf{E} \rangle + \eta_0 \frac{5}{2} \phi \langle \mathbf{E} \rangle . \tag{H.7}$$

Substitution of eq. (G.7) yields

$$\langle \boldsymbol{\sigma} \rangle = \eta_0 \langle \mathbf{E} \rangle + \eta_0 \frac{5}{2} \frac{\phi}{1-\phi} \langle \mathbf{E} \rangle \simeq \eta_0 \left(1 + \frac{5}{2}\phi \right) \langle \mathbf{E} \rangle . \tag{H.8}$$

This is the same result as obtained by Einstein. Let us now consider the volume average stress tensor for a microswimmer. As eq. (H.6) is linear in the velocity we can simply add the extra contribution of the swimmer induced field. From now on the unit vector is denoted as $\hat{n} = \hat{r}$. Any force-free microswimmer induces a stresslet in the far field

$$\vec{u} = -\frac{S}{4\pi\eta_0 r^2} P_2(\hat{p} \cdot \hat{r})\hat{r} = -\frac{D}{r^2} P_2(\hat{p} \cdot \hat{r})\hat{r} , \tag{H.9}$$

and the pressure given by

$$p = -\eta \frac{D}{r^3} P_2(\hat{p} \cdot \hat{r}) . \tag{H.10}$$

Velocity gradients occur in eq. (H.6), using the identities $\nabla \vec{r} = \mathbf{I}$, $\nabla r = \hat{r}$, $\nabla \hat{r} = 1/r(\mathbf{I} - \hat{r} \otimes \hat{r})$, $\nabla(1/r^2) = -2\hat{r}/r^2$ the gradient of the stresslet field is obtained

$$\nabla \vec{u} = -\frac{D}{r^2} \left[-2\frac{P_2(\hat{p} \cdot \hat{r})}{r^3}\hat{r} \otimes \hat{r} + \frac{P_2(\hat{p} \cdot \hat{r})}{r^3}(\mathbf{I} - \hat{r} \otimes \hat{r}) + \hat{r}\frac{\nabla P_2(\hat{p} \cdot \hat{r})}{r^2} \right] , \tag{H.11}$$

with

$$\nabla P_2(\hat{p} \cdot \hat{r}) = \frac{1}{r}3(\hat{p} \cdot \hat{r})\hat{p} \cdot (\mathbf{I} - \hat{r} \otimes \hat{r}) = \frac{1}{r}3(\hat{p} \cdot \hat{r})(\hat{p} - (\hat{p} \cdot \hat{r})\hat{r}) \otimes \hat{r} . \tag{H.12}$$

Combining these expressions to calculate the symmetric gradient

$$\nabla \vec{u} + (\nabla \vec{u})^T = -\frac{D}{r^2} \left[-2\hat{r} \otimes \hat{r} + P_2(\hat{p} \cdot \hat{r})(\mathbf{I} - \hat{r} \otimes \hat{r}) + 3(\hat{p} \cdot \hat{r}) \left(\frac{1}{2}(\hat{p} \otimes \hat{r} + \hat{p} \otimes \hat{r}) \right) - 3(\hat{p} \cdot \hat{r})\hat{r} \otimes \hat{r} \right] . \tag{H.13}$$

The first part of eq. (H.6) can thus be written as

$$-\frac{D}{r^2} \left[-2\hat{r} \otimes \hat{r} + 2P_2(\hat{p} \cdot \hat{r})\hat{r} \otimes \hat{r} + \frac{3}{2}(\hat{p} \cdot \hat{r})(\hat{p} \otimes \hat{r} + \hat{p} \otimes \hat{r}) - (\hat{p} \cdot \hat{r})\hat{r} \otimes \hat{r} \right] , \tag{H.14}$$

where $(\mathbf{I} \cdot \hat{r}) \otimes \hat{r} = \hat{r} \otimes \hat{r}$ and $[(\hat{r} \otimes \hat{r}) \cdot \hat{r}] \otimes \hat{r} = \hat{r} \otimes \hat{r}$ is used. The second part of the integral in eq. (H.6) is

$$-\eta(\vec{u} \otimes \hat{n} + \hat{n} \otimes \vec{u}) = \frac{D\eta_0}{r^2}2P_2(\hat{p} \cdot \hat{r})\hat{r} \otimes \hat{r} . \tag{H.15}$$

Combining the latter two expressions eq. (H.6) reads

$$-\frac{D\eta_0}{r^2} \int \left[-2\hat{r} \otimes \hat{r} + 3(\hat{p} \cdot \hat{r}) \left(\frac{1}{2}(\hat{p} \otimes \hat{r} + \hat{p} \otimes \hat{r}) \right) \right] d\Omega , \tag{H.16}$$

The integral involves the orientation of the microswimmer $\hat{p}$, it is independent of the applied flow field. The only second rank tensors that give a non-zero symmetric contribution by averaging over the unit sphere are $\mathbf{I}$ and $\hat{p} \otimes \hat{p}$. Thus it is clear that

$$\langle \boldsymbol{\sigma} \rangle = A\mathbf{I} + B\hat{p} \otimes \hat{p} \,. \tag{H.17}$$

The trace of the tensor is $Trace(\boldsymbol{\sigma}) = 3A + B$. Taking the inproduct with $\hat{p} \otimes \hat{p}$ yields

$$\int (A\mathbf{I} + B\hat{p} \otimes \hat{p}) : (\hat{p} \otimes \hat{p}) d\Omega = A + B \,. \tag{H.18}$$

The latter part of eq. (H.16) is zero when averaged over the unit sphere. With

$$\int (\hat{r} \otimes \hat{r}) : (\hat{p} \otimes \hat{p}) d\Omega = \frac{8\pi}{3} \,. \tag{H.19}$$

and $Trace(r \hat{\otimes} \hat{r}) = 0$ the two constants A and B can be determined, yielding a contribution to the stress:

$$4\pi\eta_0 D(\hat{p} \otimes \hat{p} - \mathbf{I}/3) \,. \tag{H.20}$$

So that

$$\langle \boldsymbol{\sigma} \rangle = \eta_0 \langle \mathbf{E} \rangle + \eta_0 \frac{5}{2}\phi \langle \mathbf{E} \rangle + S(\langle \hat{p} \otimes \hat{p} \rangle - \mathbf{I}/3) \,. \tag{H.21}$$

with S the stresslet strength.

Bibliography

[1] Bruce Alberts, Alexander Johnson, Julian Lewis, Martin Raff, Keith Roberts, and Peter Walter. *Molecular Biology of the Cell*. Garland Science, 5 edition, November 2007.

[2] G. Alexander and J. Yeomans. Hydrodynamic Interactions at Low Reynolds Number. *Experimental Mechanics*, 50(9):1283–1292, November 2010.

[3] G. K. Batchelor. The stress system in a suspension of force-free particles. *Journal of Fluid Mechanics*, 41(03):545–570, 1970.

[4] G. K. Batchelor and G. K. Batchelor. *An Introduction to Fluid Dynamics*. Cambridge University Press, February 2000.

[5] M. A. Bees, N. A. Hill, and T. J. Pedley. Analytical approximations for the orientation distribution of small dipolar particles in steady shear flows. *Journal of Mathematical Biology*, 36(3):269–298, February 1998.

[6] Matthew Bennett, Michael F. Schatz, Heidi Rockwood, and Kurt Wiesenfeld. Huygens's clocks. *Proceedings of the Royal Society of London. Series A: Mathematical, Physical and Engineering Sciences*, 458(2019):563–579, March 2002.

[7] J. Blake and A. Chwang. Fundamental singularities of viscous flow. *Journal of Engineering Mathematics*, 8(1):23–29, January 1974.

[8] J. R. Blake. A spherical envelope approach to ciliary propulsion. *Journal of Fluid Mechanics*, 46(01):199–208, 1971.

[9] H. Brenner. Rheology of a dilute suspension of dipolar spherical particles in an external field. *Journal of Colloid and Interface Science*, 32(1):141–158, January 1970.

[10] F. P. Bretherton. The motion of rigid particles in a shear flow at low Reynolds number. *Journal of Fluid Mechanics*, 14(02):284–304, 1962.

[11] C. J. Brokaw. Flagellar movement: a sliding filament model. *Science (New York, N.Y.)*, 178(60):455–462, November 1972.

[12] C. J. Brokaw. Thinking about flagellar oscillation. *Cell motility and the cytoskeleton*, 66(8):425–436, August 2009.

[13] C. J. Brokaw and D. J. L. Luck. Bending patterns of chlamydomonas flagella I. Wild-type bending patterns. *Cell Motility*, 3(2):131–150, 1983.

[14] Sébastien Camalet and Frank Jülicher. Generic aspects of axonemal beating. *New Journal of Physics*, 2(1):24+, October 2000.

[15] chlamy.org. www.chlamy.org/, 2011.

[16] T. Choy. The viscosity of suspensions — an effective medium approach that incorporates Brownian motion1. *Physica A: Statistical and Theoretical Physics*, 221(1-3):263–276, November 1995.

[17] C. G. de Kruif, E. M. F. van Iersel, A. Vrij, and W. B. Russel. Hard sphere colloidal dispersions: Viscosity as a function of shear rate and volume fraction. *The Journal of Chemical Physics*, 83(9):4717–4725, 1985.

[18] Knut Drescher, Raymond E. Goldstein, Nicolas Michel, Marco Polin, and Idan Tuval. Direct Measurement of the Flow Field around Swimming Microorganisms. *Physical Review Letters*, 105(16):168101+, Oct 2010.

[19] A. Einstein. Eine neue Bestimmung der Molekueldimensionen. *Annalen der Physik*, 19:289+, 1906.

[20] A. Einstein. Berichtigung zu meiner Arbeit: Eine neue Bestimmung der Molekueldimensionen. *Annalen der Physik*, 34:591+, 1911.

[21] B. M. Friedrich, I. H. Riedel-Kruse, J. Howard, and F. Julicher. High-precision tracking of sperm swimming fine structure provides strong test of resistive force theory. *J Exp Biol*, 213(8):1226–1234, April 2010.

[22] Raymond E. Goldstein, Marco Polin, and Idan Tuval. Noise and Synchronization in Pairs of Beating Eukaryotic Flagella. *Physical Review Letters*, 103(16):168103+, Oct 2009.

[23] Jeffrey S. Guasto, Karl A. Johnson, and J. P. Gollub. Oscillatory Flows Induced by Microorganisms Swimming in Two Dimensions. *Physical Review Letters*, 105(16):168102+, Oct 2010.

[24] Brian M. Haines, Andrey Sokolov, Igor S. Aranson, Leonid Berlyand, and Dmitry A. Karpeev. Three-dimensional model for the effective viscosity of bacterial suspensions. *Physical Review E*, 80(4):041922+, Oct 2009.

[25] Elizabeth Harris. *The Chlamydomonas Sourcebook*. Academic Press, November 2008.

[26] Yashodhan Hatwalne, Sriram Ramaswamy, Madan Rao, and R. Aditi Simha. Rheology of Active-Particle Suspensions. *Physical Review Letters*, 92(11):118101+, Mar 2004.

[27] Sebastian Heidenreich, Siegfried Hess, and Sabine H. L. Klapp. Non-linear rheology of active particle suspensions: Insights from an analytical approach. *Phys. Rev. E*, 83, Nov 2011.

[28] N. Hill. A Biased Random Walk Model for the Trajectories of Swimming Micro-organisms. *Journal of Theoretical Biology*, 186(4):503–526, June 1997.

[29] E. J. Hinch and L. G. Leal. The effect of Brownian motion on the rheological properties of a suspension of non-spherical particles. *Journal of Fluid Mechanics*, 52(04):683–712, 1972.

[30] Jonathon Howard. *Mechanics of Motor Proteins and the Cytoskeleton*. Sinauer Associates, February 2001.

[31] innovatieplatform. Algencultuur op drainwater uit de glastuinbouw - Naar een pilot algenteelt voor de glastuinbouw , September 2009.

[32] innovatieplatform. Delfzijl breeding ground for green materials for coatings, September 2009.

[33] Takuji Ishikawa and T. J. Pedley. The rheology of a semi-dilute suspension of swimming model micro-organisms. *Journal of Fluid Mechanics*, 588:399–435, 2007.

[34] Takuji Ishikawa, M. P. Simmonds, and T. J. Pedley. Hydrodynamic interaction of two swimming model micro-organisms. *Journal of Fluid Mechanics*, 568(-1):119–160, 2006.

[35] J.Dunkel. Private communication, 2011.

[36] G. B. Jeffery. The Motion of Ellipsoidal Particles Immersed in a Viscous Fluid. *Proceedings of the Royal Society of London. Series A*, 102(715):161–179, November 1922.

[37] M. S. Jones, L. Le Baron, and T. J. Pedley. Biflagellate gyrotaxis in a shear flow. *Journal of Fluid Mechanics*, 281:137–158, 1994.

[38] R. B. Jones. Spherical particle in Poiseuille flow between planar walls. *The Journal of chemical physics*, 121(1):483–500, July 2004.

[39] John O. Kessler. Hydrodynamic focusing of motile algal cells. *Nature*, 313(5999):218–220, January 1985.

[40] Irvin M. Krieger. A Mechanism for Non-Newtonian Flow in Suspensions of Rigid Spheres. *Journal of Rheology*, 3(1):137–152, 1959.

[41] L. D. Landau and E. M. Lifshitz. *Fluid Mechanics, Second Edition: Volume 6 (Course of Theoretical Physics)*. Course of theoretical physics / by L. D. Landau and E. M. Lifshitz, Vol. 6. Butterworth-Heinemann, 2 edition, January 1987.

[42] Eric Lauga and Thomas R. Powers. The hydrodynamics of swimming microorganisms. *Reports on Progress in Physics*, 72(9):096601+, September 2009.

[43] James Lighthill. Flagellar Hydrodynamics: The John von Neumann Lecture, 1975. *SIAM Review*, 18(2):161–230, 1976.

[44] M. J. Lighthill. On the squirming motion of nearly spherical deformable bodies through liquids at very small reynolds numbers. *Comm. Pure Appl. Math.*, 5(2):109–118, 1952.

[45] C. B. Lindemann. A model of flagellar and ciliary functioning which uses the forces transverse to the axoneme as the regulator of dynein activation. *Cell motility and the cytoskeleton*, 29(2):141–154, 1994.

[46] C. B. Lindemann and Kathleen A. Lesich. Flagellar and ciliary beating: the proven and the possible. *Journal of cell science*, 123(Pt 4):519–528, February 2010.

[47] I. Llopis and I. Pagonabarraga. Hydrodynamic interactions in squirmer motion: Swimming with a neighbour and close to a wall. *Journal of Non-Newtonian Fluid Mechanics*, 165(17-18):946–952, September 2010.

[48] Mohammad H. Morowvat, Sara Rasoul-Amini, and Younes Ghasemi. Chlamydomonas as a ” new” organism for biodiesel production. *Bioresource Technology*, 101(6):2059–2062, March 2010.

[49] S. Mueller, E. W. Llewellin, and H. M. Mader. The rheology of suspensions of solid particles. *Proceedings of the Royal Society A: Mathematical, Physical and Engineering Science*, December 2009.

[50] Ali Najafi and Ramin Golestanian. Simple swimmer at low Reynolds number: Three linked spheres. *Physical Review E*, 69(6):062901+, June 2004.

[51] Thomas Niedermayer, Bruno Eckhardt, and Peter Lenz. Synchronization, phase locking, and metachronal wave formation in ciliary chains. *Chaos (Woodbury, N.Y.)*, 18(3), September 2008.

[52] Mark G. Nielsen and Elizabeth C. Raff. The best of all worlds or the best possible world? Developmental constraint in the evolution of beta-tubulin and the sperm tail axoneme. *Evolution & development*, 4(4):303–315, 2002.

[53] ntr. www.ntr.nl, 2011.

[54] T. J. Pedley and J. O. Kessler. A new continuum model for suspensions of gyrotactic micro-organisms. *Journal of Fluid Mechanics*, 212(-1):155–182, 1990.

[55] Marco Polin, Idan Tuval, Knut Drescher, J. P. Gollub, and Raymond E. Goldstein. Chlamydomonas swims with two "gears" in a eukaryotic version of run-and-tumble locomotion. *Science (New York, N.Y.)*, 325(5939):487–490, July 2009.

[56] C. Pozrikidis. *Boundary integral methods for linearized viscous flow.* Cambridge University Press, November 1992.

[57] V. Prasad and Eric R. Weeks. Two-Dimensional to Three-Dimensional Transition in Soap Films Demonstrated by Microrheology. *Physical Review Letters*, 102(17):178302+, April 2009.

[58] E. M. Purcell. Life at low Reynolds number. *American Journal of Physics*, 45(1):3–11, 1977.

[59] Salima Rafai, Levan Jibuti, and Philippe Peyla. Effective Viscosity of Microswimmer Suspensions. *Physical Review Letters*, 104(9):098102+, Mar 2010.

[60] D. L. Ringo. Flagellar motion and fine structure of the flagellar apparatus in Chlamydomonas. *The Journal of cell biology*, 33(3):543–571, June 1967.

[61] U. Rüffer and W. Nultsch. High-speed cinematographic analysis of the movement of Chlamydomonas. *Cell Motility*, 5(3):251–263, 1985.

[62] David Saintillan. Extensional rheology of active suspensions. *Physical Review E*, 81(5):056307+, May 2010.

[63] R. Aditi Simha and Sriram Ramaswamy. Hydrodynamic Fluctuations and Instabilities in Ordered Suspensions of Self-Propelled Particles. *Physical Review Letters*, 89(5):058101+, Jul 2002.

[64] Geoffrey Taylor. Analysis of the Swimming of Microscopic Organisms. *Proceedings of the Royal Society of London. Series A. Mathematical and Physical Sciences*, 209(1099):447–461, November 1951.

[65] wikipedia. www.wikipedia.org, 2011.

[66] David M. Woolley. Flagellar oscillation: a commentary on proposed mechanisms. *Biological reviews of the Cambridge Philosophical Society*, 85(3):453–470, August 2010.